

Wind Vector Retrievals under Rain with Passive Satellite Microwave Radiometers

Thomas Meissner, *Member, IEEE* and Frank J. Wentz

Abstract—We have developed algorithms that retrieve ocean surface wind speed and direction under rain using brightness temperature measurements from passive microwave satellite radiometers. For accurate radiometer retrievals of wind speeds in rain it is essential to use brightness temperature signals at different frequencies, whose spectral signature makes it possible to find channel combinations that are sufficiently sensitive to wind speed but little or not sensitive to rain. The wind speed retrieval accuracy of an algorithm that utilizes C-band frequencies and is trained for tropical cyclones ranges from 2.0 m/s in light rain to 4.0 m/s in heavy rain. We have also trained and tested global algorithms that are less accurate in tropical storms but can be applied under all conditions. The wind direction retrieval accuracy degrades from about 10° in light rain to 30° at the onset of heavy rain. We compare the performance of wind vector retrievals under rain from microwave radiometers with those from scatterometers and discuss advantages and shortcomings of both instruments. We have also analyzed the wind induced sea surface emissivity including its wind direction dependence for wind speeds up to 45 m/s.

Index Terms—Microwave radiometers, ocean wind vector, rain, tropical cyclones, WindSat.

Manuscript received June 11, 2009. This work was supported in part by NASA contract no. NNH06CC29C (Ocean Products from WindSat). The authors are with Remote Sensing Systems, 438 First Street, Suite 200, Santa Rosa, CA 94501, USA (e-mail: meissner@remss.com, frank.wentz@remss.com).

I. INTRODUCTION

The measurement of ocean surface wind speeds under rain has been a long outstanding problem for passive satellite microwave radiometers. Algorithms have been developed that are able to measure ocean surface wind speeds with an accuracy of at least 1 m/s as long as the scenes are free of rain [1;2]. Unfortunately, these algorithms break down completely as soon as even only light rain is present. There are basically three reasons why it is difficult to measure radiometer wind speeds in rainy conditions:

- 1) Rain increases the atmospheric attenuation, especially at higher frequencies. The brightness temperature signal and therefore the signal to noise ratio decreases with the square of the atmospheric transmittance τ^2 . Therefore under rain the radiometer measurement is less sensitive to the surface wind speed. The rain free wind speed retrieval algorithm is a physical algorithm. It is based on either Monte-Carlo simulating brightness temperatures from a physical radiative transfer model (RTM), from which regressions for the surface wind speed as function of the measured brightness temperatures can be derived [2] or on performing a non linear optimization that minimizes the difference between measured and RTM computed brightness temperatures [1].
- 2) It is very difficult to accurately model brightness temperatures in rain. Because of the high variability of rainy atmospheres, the brightness temperatures depend on cloud type and the distribution of rain within the footprint (beamfilling) [3;4]. In addition, with increasing frequency and increasing drop size, atmospheric scattering starts to become important. That means that it is not possible to use the simple Rayleigh approximation for cloud water absorption but one rather needs to apply the full Mie absorption theory [3-5]. This requires additional input such as size and form of the rain drops. However, those parameter are not readily available.
- 3) The brightness temperature signals of rain and wind are very similar. Therefore the rain free wind speed algorithm tends to treat an increase in rain the same way as an increase in wind speed.

For many applications such as storm forecasting, it is of course highly desirable to have the ability of accurate wind speed retrievals under rain from passive satellite microwave radiometer measurements. This study is a first attempt to do that. Our analysis is based on brightness tem-

perature measurements from the WindSat radiometer (<http://www.nrl.navy.mil/WindSat/>). In order to mitigate the problems listed above, our wind speed algorithm in rain is different from the wind speed algorithm in rain free conditions in the following ways:

- 1) It uses C-band and X-band frequencies, where the atmospheric attenuation stays relatively small, even in heavy rain.
- 2) Rather than a physical algorithm that is trained with RTM simulated brightness temperatures, the core algorithm for wind speed retrievals in rain will be a statistical algorithm. That means that it is trained from a matchup set of radiometer brightness temperatures and ocean surface wind speeds, which have both been measured under rainy conditions.

The goal of training the algorithm under rainy conditions is to force it using channel combinations that reduce the signal coming from rain without reducing the wind speed signal too much. This idea has been employed in the past for radiometer instruments taking multi-frequency measurements within C-band and that were flown on aircrafts to measure wind speeds in hurricanes [6;7]. Their success gives reason to the hope that the spectral difference in the rain and wind signals between different frequency bands is also able to accomplish this goal. We will show that such an algorithm can be used for retrieving wind speeds in hurricanes to a reasonable degree of accuracy, although we cannot expect that the wind speeds have the same accuracy as in rain free cases.

We will also develop a semi-statistical algorithm that decouples the rainy atmosphere from the wind roughened ocean surface. The atmospheric transmittance τ and the up- and downwelling atmospheric brightness temperatures T_{BU} and T_{BD} , respectively, will be computed from a statistical algorithm. The surface emissivity, on the other hand, will be computed from our ocean surface emissivity model using a random wind speed distribution instead of a matchup set of radiometer brightness temperatures and ocean surface wind speeds. We will use this data set to retrieve globally wind speeds in rain. On a global scale, sufficient matchups for wind speeds above 18 m/s are not available, which necessitates the use of the semi-statistical algorithm that does not need any wind speed measurements for training.

Finally, we will also study how well a polarimetric radiometer can measure wind direction in rain. An important aspect will be to assess the performance of passive radiometers compared with active scatterometers for wind vector measurements in tropical storms and compare how much radiometer and scatterometer degrade under rain. The degradation of scatterometer wind

speed measurements is due to three effects: Rain splashing at the ocean surface leading to additional roughening, atmospheric attenuation of the backscatter signal in the rainy atmosphere and scattering by rain drops [8-10]. A common perception is that the performance of the scatterometer for retrieving wind speed and direction degrades moderately under rain, whereas the radiometer is unusable even in only light rain. This is certainly true if the radiometer retrievals were performed with a rain free algorithm [1;2]. Our study will show that when retrieving the radiometer winds with an algorithm that has been trained in rain, active and passive instruments perform on average equally well.

Our paper will be organized as follows. Section II describes the features of the various data sets that we will be using for training and testing our algorithms. In section III we will derive a basic atmospheric set for τ , T_{BU} and T_{BD} from observed brightness temperatures. In section IV we will demonstrate how to extend our wind induced sea surface emission model [2], which so far has been validated only for wind speeds below 18 m/s, to higher wind speeds. In section V we will demonstrate in a simple case study, how an algorithm that uses C-band and X-band brightness temperatures and that is trained specifically for rain, can find channel combinations that reduce the sensitivity to rain without reducing the sensitivity to wind speed. Training and testing of an algorithm for wind speed retrievals in tropical cyclones will be described in section VI and training and testing for a global wind speed algorithm under rain will be described in section VII. For both cases we will discuss how much the performance degrades if no C-band and if neither C-band nor X-band measurements are used. Section VIII will describe the basic features and performance of radiometer wind direction retrievals under rain focusing on tropical cyclones. Finally, in section IX we will compare the performance of radiometer versus scatterometer wind speed and direction measurements under rain in hurricanes. Section X summarizes our main results and conclusions.

II. STUDY DATA SETS

This section describes how we obtain the collocated data sets which we will be using for training and testing our wind vector retrieval algorithms in rain.

A. *Calibrated WindSat Brightness Temperatures in Rain*

All wind vector retrievals for this study are based on WindSat brightness temperature (TB) measurements for the years 2003 and 2004. The WindSat instrument is fully polarimetric at 10.7, 18.7 and 37 GHz with vertical (V), horizontal (H), +45° (P) and -45° (M) and left (L) and right (R) circular polarized channels. At 6.8 GHz and 23.8 GHz only V- and H-pols are measured. The polarimetric capability allows the retrieval of wind direction in addition to wind speed. We have processed Level 0 radiometer count measurements, which were provided by the Naval Research Laboratory (NRL), into calibrated Level 2 brightness temperatures following the basic on-orbit calibration outlined in [2]. In addition, we have performed a correction for the sun intrusion into the hot load [11]. The measurements of all channels have been resampled onto a common and fixed Earth grid consisting of $1/8^\circ$ latitudinal by $1/8^\circ$ longitudinal cells following the optimum interpolation (OI) method of [12;13]. Resampled brightness temperatures are produced at 4 different resolutions:

- 1) Very low resolution (VLR): It matches the resolution of the 6.8 GHz channels (about 50 km) and the resampling is done for the 6.8 10.7, 18.7, 23.8 and 37.0 GHz channels.
- 2) Low resolution (LR): It matches the resolution of the 10.7 GHz channels (about 31 km) and the resampling is done for the 10.7, 18.7, 23.8 and 37.0 GHz channels.
- 3) Medium resolution (MR): It matches the resolution of the 18.7 GHz channels (about 20 km) and the resampling is done for the 18.7, 23.8 and 37.0 GHz channels.
- 4) High resolution (HR): It matches the resolution of the 37.0 GHz channels (about 10 km) and the resampling is done for the 37.0 GHz channels.

For retrieving wind speeds and directions in rain we use VLR brightness temperatures for the C-band (6.8 GHz) channels and LR brightness temperatures for all channels between 10.7 GHz and 37.0 GHz. Resampling the C-band channels on LR rather than VLR would trade a slightly better resolution for a larger noise. As the rain absorption at C-band is small, we do not expect a significant difference in the wind vector retrieval performance whether the C-band channels are resampled at VLR or at LR.

The WindSat measurements show a squint effect in the 4th Stokes parameters at 10.7 and 18.7 GHz. Because the antenna patterns of the L and R are not exactly aligned, the 4th Stokes parameter, which is the difference between L and R brightness temperatures, can contain spurious contributions near geographic interfaces (e.g. ocean/land, rain/no-rain, cloud/cloud-free scenes).

This poses especially a problem for measuring wind direction in rain, which depends heavily on an accurate knowledge of the 4th Stokes parameters. Using the optimum interpolation described above we were able to remove this squint by shifting the relative fields of view for the L and R channels so that they are effectively aligned.

For diagnostic purposes we also retrieve the surface rain rate from the WindSat brightness temperatures by applying the Unified Microwave Ocean Retrieval Algorithm (UMORA) [3], which utilizes both the MR and the HR brightness temperatures.

In order to decide if there is rain in the cell for which we retrieve wind speed and direction we check if either the 37V or the 37H brightness temperature lies within the boundaries for typical rain free ocean scenes. If it is not, then we flag this $1/8^\circ$ grid cell as well as all 8 surrounding cells of the grid for rain contamination.

We check in each cell for each channel if there is a valid measurement of the forward looking swath. If there is one, then we use it. If there is not, we take the measurement of the backward looking swath, if it exists. If, for any channel, there is neither a for nor an aft measurement, we discard the whole cell.

For a given channel, the Earth Incidence Angle (EIA) θ varies considerably over the whole data set because of the oblateness of the Earth and also because the mounting of the WindSat instrument to the platform results in noticeable values for roll and pitch angles and therefore a variation of the at EIA across each scan [14;15]. The difference between the maximum and the minimum EIA values gets close to 1.5° . It is therefore necessary to shift all TB observations of a given channel i to a common reference EIA $\theta_{\text{ref}, i}$.

B. WindSat Brightness Temperatures over NCEP GDAS Wind Vectors and SSM/I Atmospheres

This data set will be used in section VII for training and testing of a wind speed retrieval algorithm that can be applied globally and under all existing rain conditions and low wind speeds. We collocate WindSat brightness temperatures with wind vectors from the final analyses of the National Centers for Environmental Prediction (NCEP) General Data Assimilation System (GDAS), which are provided in 6 hour time intervals on a 1° latitudinal by 1° longitudinal grid. The NCEP zonal and meridional wind vector components u and v , respectively, are tri-linearly interpolated to the time of the WindSat measurement and to the latitude and longitude of the $1/8^\circ$

WindSat Earth grid cell center. For a variety of purposes it is beneficial to have measurements for atmospheric parameters (columnar water vapor V and surface rain rate R) from an independent instrument available. Because the ascending node times of WindSat and the Special Sensor Microwave Imager (SSM/I) [16] that is flying on platform F13, are within less of 1 hour of each other, we can collocate the WindSat TB, the NCEP GDAS wind vector field u, v and the F13 SSM/I columnar vapor V and rain rate R , if the measurement times of WindSat and F13 differ by less than 60 minutes. The SSM/I product is produced by Remote Sensing Systems' version 6 algorithm (see <http://www.remss.com>). We include an observation into the data set only if the WindSat TB rain flag indicates rain, as it was explained in section II.A. Collocations are performed over the full 2 years of 2003 and 2004. The whole data set comprises about 4 million events. The data set also includes NCEP GDAS atmospheric profiles for temperature, pressure and water vapor density that are tri-linearly interpolated to the location and time of the WindSat measurement. The water vapor density profiles are scaled so that its total vertical integral equals the total columnar water vapor V from F13 SSM/I [2;17;18].

C. *WindSat Brightness Temperatures over HRD Wind Vectors*

This data set will be used for training and testing wind vector retrieval algorithms under conditions that are present in tropical cyclones. For this purpose, we have collected WindSat passes over wind fields supplied by NOAA's Hurricane Research Division of AOML (HRD) (<http://www.aoml.noaa.gov/hrd/index.html>). The HRD wind vectors analysis is based on ground observations (buoys, ships), aircraft observations, various satellite measurements and the use of pressure – wind relationships [19]. We are using data from 17 hurricanes during 2003 and 2004. For a valid collocation we compute the time average of all WindSat observations that fall onto the locations of the HRD field and demand that the time of the HRD analysis and the average time of the WindSat overpass are within 3 hours. No temporal interpolation between HRD analyses at different times is performed as the time intervals are too large in most cases.

The HRD wind fields are given on a very high resolution, which is about 5 km. In order to compare the HRD field with the WindSat observation, it is necessary to have both of them approximately at the same resolution. Therefore we need to resample the HRD wind field to the WindSat LR resolution, which matches the size of the X-band 3 dB (half power) footprint ($2r_0 = 31$ km) at each of the $1/8^\circ$ WindSat Earth grid cells. If r is the distance from the center

y of a WindSat Earth grid cell to the center x of the original HRD field components $u_{\text{HRD}}(x)$ and $v_{\text{HRD}}(x)$, then the resampled HRD field components $u_{\text{HRD}}^{\text{resampled}}(y)$ and $v_{\text{HRD}}^{\text{resampled}}(y)$ at the location y of the WindSat cell are computed as weighted averages:

$$u_{\text{HRD}}^{\text{resampled}}(y) = \frac{\sum e^{-\ln 2 \left(\frac{r}{r_0}\right)} \cdot u_{\text{HRD}}(x)}{\sum e^{-\ln 2 \left(\frac{r}{r_0}\right)}} \quad v_{\text{HRD}}^{\text{resampled}}(y) = \frac{\sum e^{-\ln 2 \left(\frac{r}{r_0}\right)} \cdot v_{\text{HRD}}(x)}{\sum e^{-\ln 2 \left(\frac{r}{r_0}\right)}} \quad (1)$$

The sum \sum runs over all of the original HRD fields which are sufficiently close to the center of the WindSat Earth cell to give a finite contribution to the whole sum. The use of the simple resampling form (1) is based on the fact that the brightness temperature and therefore the power that is received falls roughly off exponentially with the distance from the center being reduced by half at $2r_0 = 31$ km and that the wind speed is roughly proportional to the brightness temperature. We want to note already at this point that the resampling (1) will necessarily smear out some of geophysical feature of the hurricane, as it can be seen when plotting the resampled HRD wind fields (Figure 4(a) and Figure 9(c)). For example, the eyes with low wind speeds in the center of the hurricanes are barely visible in the resampled HRD fields.

Within the 3 hour time window between the time of the HRD analysis and the time of the WindSat observation the hurricane can have moved over a considerable distance which could introduce a significant error in our analysis. In order to minimize this error, we have shifted the HRD wind vector field for each storm in the data set so that the eye of the HRD field coincides with the eye of the WindSat measurement. We find the values of the shift by visually comparing the HRD field with the WindSat field.

The radiometer brightness temperature is directly sensitive to surface roughness rather than wind speed. The HRD analysis reports peak wind speeds for 1 minute sustained winds. In order to produce the surface roughness of the satellite observation the surface winds need to be sustained for longer time periods, at least 10 minutes. We use a scale factor of 0.88, which has been derived and is used by the US Navy [20], in order to convert from 1 minute sustained HRD wind speeds to 10 minute sustained satellite wind speeds.

Table 1 lists the storms that were used in the data set, the times of the HRD analysis together with the average times of the WindSat overpasses and the latitudinal and longitudinal shifts of

the storm eye. The whole data set comprises about 48,000 collocations. Every 2nd observation is used for algorithm training and the other half of the set is used for algorithm testing and validation.

Table 2 shows the population and average rain rates for the whole data set as function of wind speed. It is evident that there is a strong correlation between wind speed and rain rate and the rain rate increases with increasing wind speed.

D. WindSat Brightness Temperatures over HRD Wind Vectors and QuikSCAT Wind Vectors

In order to compare wind vector retrieval performance of radiometers and scatterometers in rain we use triple matchups of wind vectors from HRD, WindSat and the NASA scatterometer QuikSCAT [21]. This data set is a subset of the HRD – WindSat collations from section II.C. The ascending node times of WindSat and QuikSCAT are about 12 hours apart, which results in a very good time match between the ascending (descending) WindSat and the descending (ascending) QuikSCAT swaths over the equatorial region. For a valid triple matchup between WindSat, QuikSCAT and HRD we demand that each of the mutual differences between the WindSat measurement time, the QuikSCAT measurement time and the HRD analysis time are smaller than 3 hours. For our analysis we use QuikSCAT wind vectors that have been produced by the Jet Propulsion Laboratory (JPL) [22].

We do not take data from a hurricane if the HRD analysis has used QuikSCAT measurements from this storm as input. The average time difference between the WindSat and the QuikSCAT overpasses is less than 30 minutes. Therefore the dislocation between the WindSat and QuikSCAT measurements is very small and we do not need to shift the storm centers of the QuikSCAT relative to the WindSat observation. Storms, times and cell shifts for the WindSat – QuikSCAT – HRD matchups are included in Table 1. The data set contains about 16,000 events.

E. Sampling Mismatch Errors Between HRD and Satellite Winds

As explained earlier, we have shifted the HRD fields so that the eyes of the HRD hurricanes coincide with those of WindSat and QuikSCAT. Even after this shift in location there can still be sampling mismatch between the two fields, because there can be a time difference of up to 3 hours between the HRD analysis and the satellite measurement. The second column in Table 3

lists the average time differences between the observations of the various data sets. Within these time windows the hurricane can change in size and intensity. This creates a sampling mismatch error between HRD and satellite wind fields, which we need to estimate. In a few cases, HRD produces analysis fields of the same storm that are 3 hours apart. Though those cases rarely coincide with an actual satellite overpass, we can still use them for making a general estimate of the size of the errors in wind speed and direction errors due to this sampling mismatch. We first shift the HRD fields so that the storm eyes of the different HRD fields that are 3 hours apart, coincide. We then calculate the RMS of the wind speed and direction differences between these two analysis fields. We find that the RMS of the wind speed difference between two storms that are 3 hours apart amounts to approximately 2.0 m/s and the RMS wind direction difference amounts to about 20° . In order to estimate the RMS differences for the sampling mismatches in Table 3, we scale the squares of these RMS values from the full 3 hours to the average time differences between HRD and satellite that are listed in the second column of Table 3. The results are the third column. When assessing the performance of our algorithms by computing statistics for WindSat – HRD and QuikSCAT – HRD wind speed and direction differences we will back out those estimated sampling mismatch errors in an RMS sense.

III. BASIC GLOBAL ATMOSPHERIC SET AND AUXILIARY ATMOSPHERIC ALGORITHMS

A. *Derivation of the Basic Global Atmospheric Set*

The basic global atmospheric set comprises the whole data set of section II.B containing 2 full years of WindSat TB from raining ocean scenes and NCEP GDAS wind vectors that are collocated with F13 SSM/I water vapor and rain rate measurements within a 60 minute time window. The goal is to derive the values for the atmospheric transmittance τ and the upwelling and downwelling atmospheric brightness temperatures T_{BU} and T_{BD} , respectively. As mentioned earlier calculating these parameters from atmospheric profiles using a rain absorption model is very difficult. However, they can be determined at each frequency from the WindSat dual polarization brightness temperature measurements. The top of the atmosphere brightness temperature (TOA TB) $T_{B,p}$ at polarization $p = V, H$ is:

$$\begin{aligned}
T_{B,p} &= T_{BU} + \tau (1-R_p) T_S + (1+\Omega_p) \tau R_p (T_{BD} + \tau T_C) - \tau \Omega_p R_p T_C \\
&= T_U (1-\tau) + \tau (1-R_p) T_S + (1+\Omega_p) \tau R_p [T_D (1-\tau) + \tau T_C] - \tau \Omega_p R_p T_C
\end{aligned} \tag{2}$$

In equation (2), R_p denotes the reflectivity for polarization p , T_S is the sea surface temperature, T_C is the cold space temperature and Ω_p an empirical correction for downwelling radiation that is reflected from the surface from non-specular directions [23]. The reflectivity R_p depends on frequency ν , sea surface temperature T_S and salinity s , sea surface wind speed W , surface wind direction relative to the azimuthal look ϕ_r and the Earth incidence angle (EIA) θ . $T_U \equiv \frac{T_{BU}}{(1-\tau)}$ and

$T_D \equiv \frac{T_{BD}}{(1-\tau)}$ are the upwelling and downwelling atmospheric temperatures, respectively. For non

scattering atmospheres, T_{BU} and T_{BD} can be calculated from the atmospheric profile integrals:

$$\begin{aligned}
T_{BU} &= \sec(\theta) \int_0^H dh \alpha(h) T(h) \tau(h,H) \\
T_{BD} &= \sec(\theta) \int_0^H dh \alpha(h) T(h) \tau(0,h)
\end{aligned} \tag{3}$$

In equation (3), h is the altitude in the vertical profile, $\alpha(h)$ is the total atmospheric absorption coefficient and $T(h)$ is the atmospheric temperature at altitude h . H denotes the value of h at the TOA. The atmospheric transmittance between altitude h_1 and h_2 is the integral:

$$\tau(h_1, h_2) = \exp\left(-\sec(\theta) \int_{h_1}^{h_2} dh \alpha(h)\right) \tag{4}$$

and the full atmospheric transmittance is: $\tau = \tau(0,H)$.

We start out with a simplification assuming the that the vertical atmospheric temperature profile $T(h)$ is isothermal and therefore independent on h and that it is also equal to the surface temperature T_S :

$$T(z) = T_S \equiv T_{\text{eff}} \tag{5}$$

If we also make the approximations $\Omega_p = 0$ and $T_C = 0$ and if there is no scattering, then equa-

tion (2) then reduces to

$$\begin{aligned} T_{\text{BV}} &= (1 - R_{\text{V}}\tau^2) T_{\text{eff}} \\ T_{\text{BH}} &= (1 - R_{\text{H}}\tau^2) T_{\text{eff}} \end{aligned} \quad (6)$$

If there is scattering rain in the atmosphere due to rain, the expressions (6) remain still valid but the effective temperature T_{eff} is smaller than the atmospheric temperature [3;4;24]. This temperature depression increases with increasing rain rate, decreasing absorption and increasing frequency. If both T_{BV} and T_{BH} are measured and the reflectivities R_{p} are known, we can solve the two equations (6) for the 2 unknowns τ and T_{eff} giving:

$$\tau^2 = \frac{T_{\text{B,V}} - T_{\text{B,H}}}{T_{\text{B,V}} R_{\text{H}} - T_{\text{B,H}} R_{\text{V}}} \quad (7)$$

This can be done for non raining as well as for raining atmospheres. We compute the reflectivity $R_{\text{p}}(\nu, \theta; T_{\text{s}}, s, W, \varphi_{\text{r}})$ using the sea surface temperature from the Reynolds OI product [25], sea surface salinity from the climatology from the World Ocean Atlas (WOA98, N.O.D.C, CD-ROM), and surface wind speed and direction from NCEP GDAS.

For the more refined calculation, we use the value for τ from (7) as first guess. We can then easily calculate a value for Ω_{p} , which depends on ν, θ, τ and W [23]. The next step is to calculate values for τ , T_{BU} and T_{BD} from the NCEP GDAS atmospheric profiles and the F13 columnar water vapor assuming that the atmospheres contains no rain or liquid cloud water. The real values for τ , T_{BU} and T_{BD} for the rainy atmospheres are of course very different. However, the difference $T_{\text{D}} - T_{\text{U}}$, which itself is only in the order of 1 - 2 K for the frequencies of interest, is largely independent on how much rain or cloud water the atmosphere contains and the temperature depression due to scattering is approximately the same for T_{U} and T_{D} . It is therefore justified to use the value for $T_{\text{D}} - T_{\text{U}}$ without clouds or rain also for the raining atmospheres in the basic global atmospheric set. We are then effectively left with 2 unknowns, τ and T_{U} , in the 2 equations of (2) for V- and H-pol, which we can solve and thus determine the desired values for τ , T_{BU} and T_{BD} of the whole data set of section II.B. As this set comprises 2 full years of global WindSat measurements in rain, it contains a large variety of different possible atmospheric conditions for raining atmospheres.

Once we have derived the values of τ , T_{BU} and T_{BD} for data set of section II.B from the measured V-pol and H-pol brightness temperatures, we combine it with uniform random wind speeds between 0 and 50 m/s and uniform random relative wind directions between 0° and 360° creating a synthetic data set that decouples the atmospheric from the surface effects. We compute the brightness temperatures of this synthetic data set from the radiative transfer equation (2) and our surface emissivity model [2;18]. When training global regression algorithms at high wind speeds we will use this synthetic global data instead of the WindSat TB – NCEP GDAS wind speed matchups of section II.B. The numerical weather forecast product does not include sufficient high wind speed populations so that it can be used for training a global algorithm.

B. Auxiliary Algorithms for the Atmospheric Parameters

Our wind speed and wind vector retrievals in rain will use the value of the atmospheric transmittance τ as input. We will also need the values of τ , T_{BU} and T_{BD} for the analysis of the wind induced sea surface emissivity at high wind speeds in section IV. In order to obtain τ from the WindSat brightness temperature we use the synthetic global atmospheric data set described in the last section in order to train auxiliary linear regressions of the form:

$$\tau_\nu = a_\nu(T_S) + \sum_j c_{\nu j}(T_S) \cdot (T_{B,j} - 150K) + \sum_j d_{\nu j}(T_S) \cdot (T_{B,j} - 150K)^2 \quad (8)$$

τ_ν is the transmittance at frequency ν . The sum \sum_j runs over all WindSat channels in the bands that are available for the regression. We allow the regression coefficients a_ν , $c_{\nu j}$, $d_{\nu j}$ to depend on T_S . The value of T_S is obtained from the Reynolds optimum interpolated (OI) SST product [25]. Separate regressions are trained for separate overlapping T_S bins and when retrieving τ_ν we interpolate to the actual value of T_S between the appropriate bins. We have computed τ from (8) for the WindSat – HRD matchup set (section II.C) and included the results in Table 2. Regression algorithms of the same form as (8) can be derived and trained for T_{BU} and T_{BD} .

The training of the algorithms with the synthetic data set will result in channel combinations in (8) that try to minimize the impact of the surface wind speed and therefore also minimize the systematic crosstalk between the error in the atmospheric parameters and wind speed. This will be important in the next section for the determination of the wind induced sea surface emissivity.

IV. WIND INDUCED SEA SURFACE EMISSIVITY AT HIGH WIND SPEEDS

A. Basic Method for the Determination of the Wind Induced Sea Surface Emissivity Signal

Because in tropical cyclones rain is strongly correlated with high wind events we need to determine the wind induced sea surface emissivity signal at high wind speeds before developing the wind vector retrieval algorithms in rain. In [2] both the isotropic (direction independent) and the four Stokes parameters of the wind direction signal were obtained from WindSat brightness temperature measurements and NCEP GDAS wind vectors in rain free atmospheres. This automatically limits the wind speeds to values below 18 m/s, because the range above this value is not sufficiently populated. Using the WindSat TB – HRD wind vector collocations from section II.C we can extend the wind speed range to about 45 m/s. After the resampling (equation (1)) and scaling to 10 minute sustained winds the number of HRD wind speeds that are higher than 45 m/s is getting too sparse in order to extend our analysis beyond that range.

The basic procedure is to solve the RTM equation (2) for the emissivity $E_p = 1 - R_p$ and subtract the specular sea surface emissivity E_0 , which is computed from the dielectric constant of sea water [18]. The values for the atmospheric parameters τ , T_{BU} and T_{BD} are calculated from the auxiliary atmospheric regression of section III.B.

B. Isotropic Wind Induced Emissivity

Figure 1 shows the results for the isotropic (wind direction independent) part of the wind induced sea surface emissivity at all 10 V-pol and H-pol channels as function of the HRD wind speed. The HRD wind speed range is between 10 m/s and 45 m/s and the measurements have been averaged into wind speed intervals that are between 4 m/s and 6 m/s wide. The error bars are the standard deviations of the distribution of the computed emissivity values in each bin. The solid lines are the curves from [2], which have been linearly extrapolated from 18 m/s to higher wind speeds. It is evident that the values from this analysis, which uses the WindSat brightness temperatures – HRD wind speed collocations, line up very well with the results from [2] if the wind speed is below 18 m/s. With increasing frequency the scatter in the data points increases due to increasing error in the atmospheric parameters. As mentioned in section III.B it is important that there is no correlation between the error in the atmospheric parameters and surface wind

speed.

Our results in Figure 1 show that the calculated emissivity values are consistent with a linear extrapolation of the RTM in [2] for wind speeds up to 45 m/s. At high wind speeds the increase of the surface roughness and emissivity is mainly caused by emission from sea foam. The sea foam coverage and therefore the emissivity gets larger with larger wind speed. It is expected that at high enough the wind speeds the ocean surface is completely covered with foam and therefore the emissivity signal should saturate as function of wind speed. The curves in Figure 1 do not indicate any saturation of the emissivity signal $\partial T_B / \partial W$ for wind speeds below 35 m/s but rather the signal keeps increasing with wind speed. This indicates that accurate wind speed retrievals should be feasible at least up to 35 m/s as long as the atmospheric attenuation does not get too large. Above 35 m/s Figure 1 indicates a possible saturation of the wind induced emissivity signal, especially for the lower frequencies. Due to the limited data volume and the knowledge error in the wind speed itself in that region, our analysis is not yet conclusive.

C. Wind Direction Signal for Third and Fourth Stokes Parameters

The wind direction signal is a crucial input for the retrieving wind direction from polarimetric brightness temperature measurements. In order to determine the V-pol and H-pol wind direction signals it is necessary to subtract the large wind direction independent (isotropic) contribution from the measured brightness temperatures in equation (2), which requires a very accurate knowledge of the atmospheric parameters τ , T_{BU} and T_{BD} . Even small errors in these parameters can easily swamp the small wind direction signal, which is only in the order of a few Kelvin [26]. For the rain free cases in [2], this problem can be avoided by taking the differences between forward and backward observations at the same Earth location. This method is based on the assumption that the atmosphere in the forward observation is the same as in the backward observation and therefore the large isotropic part cancels when taking the difference between for and aft looks. Because the vast number of high wind speed events contains also significant amounts of rain and the high variability of rain can cause different atmospheric conditions between the times of the for and aft observations, this assumption might not be valid for the cases that we use in our study. Therefore, we will only determine the 3rd (S3) and 4th (S4) Stokes parameters and use them for retrieving wind directions in rain.

Figure 2 shows the results for the surface signals of S3 and S4 at 10.7 GHz in seven wind speed intervals between 0 and 40 m/s. The highest wind speed interval is 10 m/s wide and all the other intervals are 5 m/s wide. Equation (6) implies that the surface signal ΔE_p and the TOA TB signal $\Delta T_{B,p}$ are approximately related by

$$\Delta T_{B,p} \approx \Delta E_p \tau^2 T_{\text{eff}} \quad (9)$$

The value for the transmittance τ is again found using the regression (8) from section III.B. For the effective atmospheric temperature we take the average between surface and freezing temperature. The solid lines in Figure 2 are the 2nd order harmonic fits of the surface emissivity signal ΔE_p as even function of the relative wind direction φ_r :

$$\Delta E_p(W, \varphi_r) = A_p^1(W) \cdot \sin(\varphi_r) + A_p^2(W) \cdot \sin(2\varphi_r), \quad p = S3, S4 \quad (10)$$

Similar curves and fits can be obtained for the other 2 polarimetric WindSat frequencies 18.7 and 37.0 GHz. The harmonic coefficients $A_p^i(W)$, $i = 1, 2$, $p = S3, S4$ depend on wind speed W and are plotted in Figure 3 for all 3 polarimetric frequencies. The dashed-dot-dot and dashed lines are polynomial fits to the data.

The results of our analysis for $A_{S3}^i(W)$, $i = 1, 2$ agree well with the findings of [2] below 20 m/s and of [27] between 20 and 40 m/s, the differences being less than 1 sigma of the spread in the measurements, as indicated by the vertical bars in Figure 2.

Our analysis shows no significant size of both harmonic coefficients of S4 at 37.0 GHz over the whole wind speed range, which is again consistent with [2] for wind speeds below 18 m/s. For the 2 lower polarimetric frequencies (10.7 and 18.7 GHz) it was found [2;28] that S4 is almost a pure 2nd harmonic below 18 m/s. That means that the curves for ΔE_p as function of φ_r are proportional to $\sin(2\varphi_r)$ and therefore the harmonic coefficient A_{S4}^1 in (10) is zero. Figure 2 and Figure 3 indicate a small 1st harmonic admixture, i.e. a small term proportional to $\sin(\varphi_r)$ in ΔE_p of S4 at 10.7 GHz at high wind speeds. Its deviation from zero is within the 1 sigma of the measurement spread. At this point it is not clear if this effect is an artifact of our analysis or real. In the following we will set A_{S4}^1 to zero at all frequencies and at all wind speeds.

The most important feature of these results for the wind direction emissivity signal is the fact

that at high winds the dominant contribution A_{S3}^1 keeps increasing with wind speed up to at least 40 m/s. In the wind speed interval between 30 and 40 m/s the peak to peak amplitude in the surface signal of S3 is about 5 K at 10.7 GHz, 6 K at 18.7 GHz and 8 K at 37.0 GHz. The surface signal of S4 at 10.7 GHz and 18.7 GHz saturates with wind speed but at least it does not decrease at high winds. This indicates that the wind direction signal has sufficient strength in hurricanes where the atmospheric attenuation is large due to rain but the wind speeds and therefore the directional signals at the surface are also large. This observation is the basis for the capability of the polarimetric WindSat radiometer to retrieve wind directions under rain in hurricanes, as we will see in section VIII and section IX.

V. THE SPECTRAL DIFFERENCE IN WIND AND RAIN SIGNATURES AND ITS UTILIZATION FOR WIND SPEED RETRIEVALS UNDER RAIN

A. Wind Speed Retrievals with the Algorithm for Non-Raining Atmospheres in Rain

Figure 4 shows wind speeds and rain rate for the WindSat pass over hurricane FABIAN on 03 September 2003. It is evident that the algorithm from [2], which was trained for non-raining atmospheres and accurately retrieves wind speeds to about 1 m/s if rain is absent, images mainly rain instead of wind speed (Figure 4 (c)). Though the color scale does not exhibit it, the largest wind speeds from this algorithm exceed 100 m/s. The reason for these large errors is that the wind speed signal in the measured brightness temperatures is very similar to the rain signal and therefore the algorithm from [2] treats an increase in rain the same way as an increase in wind speed. This also becomes clear from the bias and RMS between the retrieved WindSat wind speed and the HRD wind speed in Table 4. Table 5, which shows the bias and RMS between the WindSat and the NCEP GDAS wind speeds as function of rain rate for the global data set of section II.B, reveals that the degradation of the no-rain algorithm is already significant already in light rain.

B. Radiative Transfer Model Considerations

In order to retrieve wind speeds in rain we need to be able to find appropriate combinations of WindSat channels that reduce the sensitivity to rain without reducing the sensitivity to wind too much. As a first attempt one might consider the channel combinations $\lambda \cdot T_{BV} - T_{BH}$ between V-

pol and H-pol in each band. From the simplified RTM (6) we see that if we choose $\lambda \approx R_H/R_V$ the contribution coming from the atmospheric transmittance τ cancels. For the WindSat frequencies and Earth incidence angles this ratio R_H/R_V lies roughly between 1.5 and 1.8. Similar V-pol and H-pol channel combinations have been used in previous studies to reduce the influence of atmospheric uncertainties on the brightness temperatures [14;26]. However, from the dashed line in Figure 5 (b) we see that this combination has very little sensitivity to wind speed above 8 m/s and is therefore not suited for retrieving higher wind speeds in rain.

A better way is to combine channel combinations from different frequency bands. We demonstrate this for the H-pol channels at C-band (6H) and X-band (10H). The H-pol reflectivities are approximately the same for both frequencies $R_{6H} \approx R_{10H} \equiv R_H$. From (6) we find therefore for an arbitrary parameter λ :

$$T_{BH}^{6.8 \text{ GHz}} - \lambda \cdot T_{BH}^{10.7 \text{ GHz}} \approx - T_{\text{eff}} R_H \left(\tau_{6.8 \text{ GHz}}^2 - \lambda \cdot \tau_{10.7 \text{ GHz}}^2 \right) \quad (11)$$

λ is chosen so that the difference in (11) shows minimal sensitivity to the rain rate R . That means:

$$\frac{\partial}{\partial R} \left(\tau_{6.8 \text{ GHz}}^2 - \lambda \cdot \tau_{10.7 \text{ GHz}}^2 \right) = 0 \quad (12)$$

or

$$\lambda = \frac{\partial \tau_{6.8 \text{ GHz}} / \partial R}{\partial \tau_{10.7 \text{ GHz}} / \partial R} \quad (13)$$

From the curves of Figure 5 (a) which displays the dependence of τ^2 on R for the basic global atmospheric set, we estimate $\lambda \approx 1/3$. The solid line in Figure 5 (b) indicates that the combination

$T_{BH}^{6.8 \text{ GHz}} - \frac{T_{BH}^{10.7 \text{ GHz}}}{3}$ is sensitive to wind speed, albeit the sensitivity is smaller than for the pure 10H.

C. Training of a Statistical Regression Algorithm for Raining Atmospheres

The optimal combination between 6H and 10H is found in a least square sense by training a linear regression:

$$W = c_0 + c_{6H} \cdot T_{BH}^{6.8 \text{ GHz}} + c_{10H} \cdot T_{BH}^{10.7 \text{ GHz}} \quad (14)$$

The result for the regression coefficients in (14) is: $c_0 = -35.4$, $c_{6H} = 0.76$, $c_{10H} = -0.22$, which means that $c_{10H} \approx -0.3 \cdot c_{6H}$. This is close to the ratio λ from the last section. Retrieving the wind speed using the simple combination (14) results in a strong improvement over the no-rain algorithm as it is immediately obvious from Figure 4 (e) and from Table 4. That means that we were able to utilize the spectral differences in wind and rain signatures in order to remove the rain signal but still keeping sufficient sensitivity to wind speed.

Our algorithm for retrieving wind speeds in rain is based on this principle. Rather than using only the two channels 6H and 10H as in (14), we will utilize all WindSat channels. This will improve the retrieval accuracy. The optimal configuration that minimizes the retrieval error can be again determined by training appropriate linear regressions.

VI. H-WIND SPEED ALGORITHM FOR TROPICAL CYCLONES

The WindSat H-wind algorithm is trained from the WindSat TB – HRD wind speed matchups (section II.C) and its purpose is to retrieve wind speeds in conditions that are typical for tropical cyclones. It has the form:

$$W = a(\tau_{10.7 \text{ GHz}}) + b(\tau_{10.7 \text{ GHz}}) \cdot T_S + \sum_j c_j(\tau_{10.7 \text{ GHz}}) \cdot (T_{B,j} - 150\text{K}) + \sum_j d_j(\tau_{10.7 \text{ GHz}}) \cdot (T_{B,j} - 150\text{K})^2 \quad (15)$$

The sum \sum_j runs over all V-pol and H-pol channels in the frequency bands that are available for the regressions. Including the polarimetric channels does not lead to a significant increase in performance. The value of the sea surface temperature T_S is obtained from the Reynolds OI product [25]. The regression coefficients a , b , c_j , d_j depend on the atmospheric transmittance at 10.7 GHz $\tau_{10.7 \text{ GHz}}$. Separate regressions are trained for separate overlapping τ bins. That

means effectively that the weighting of the channels is different for atmospheres with high rain than for atmospheres with heavy rain. When running the algorithm, we first calculate $\tau_{10.7\text{ GHz}}$ from (8) and then interpolate to the actual value of $\tau_{10.7\text{ GHz}}$ between the appropriate bins. Equivalently, we could use the rain rate R for labeling the regression coefficients rather than $\tau_{10.7\text{ GHz}}$, as both R and $\tau_{10.7\text{ GHz}}$ contain basically the same input information. In practice, when running a wind speed retrieval, obtaining $\tau_{10.7\text{ GHz}}$ from the auxiliary algorithm (8) is a technically easier than retrieving R from the UMORA rain algorithm [3].

We have trained and tested an algorithm that utilizes all five WindSat frequency bands (called C-band algorithm), an algorithm that does not utilize C-band (called X-band algorithm) and an algorithm that utilizes neither C-band nor X-band (called K-band algorithm). The reason for studying X-band and K-band algorithms is that those algorithms could be used to produce wind speeds at higher resolution (LR or MR) and that they could be applied at microwave instruments without the lower bands. For example an X-band algorithm could be developed for the Tropical Rainfall Measuring Mission (TRMM) Microwave Imager (TMI) or a K-band algorithm could be developed for the SSM/I or its follow up instruments SSMIS.

Figure 4 (g) – (i) show the retrieved wind speed fields from the three H-wind algorithms for the WindSat pass over hurricane FABIAN. In Figure 6 we have plotted the bias and standard deviation of the difference between the WindSat H-wind speed and the HRD wind speed as function of the rain rate. The estimated sampling mismatch error between WindSat and HRD winds has been removed as explained in section II.E. From Figure 6 we see that the for rain rates below 5 mm/h, the performance of the X-band algorithm is as good as the performance of the C-band algorithm. For heavier rain the X-band algorithm degrades moderately from the C-band algorithm. The degradation of the K-band algorithm occurs already in light rain, resulting in noticeably larger standard deviations than the C-band or X-band algorithms (lower panel of Figure 6). This is not unexpected. First of all, a statistical algorithm like the H-wind algorithm performs better the more channels are available. Moreover, the attenuation increases with frequency (Table 2) and the larger the attenuation is the smaller is the signal to noise ratio, which translates into a larger retrieval error. However, it also obvious that even the K-band H-wind algorithm still constitutes a strong improvement over the no-rain algorithm (Figure 4 (c)). In Figure 4 (g) – (i) we can still recognize some residual error in the wind speeds due to rain contamination. We can see that in some cases the H-wind algorithms either undercorrect or overcorrect the rain effect.

This depends on rain rate but can also depend on wind speed itself. For example, the H-wind C-band algorithm slightly underestimates the wind speeds in the high wind region near the storm center and slightly overestimates the wind speed in the outer rain bands. This error is part of the standard deviation error in the lower panel of Figure 6. As the upper panel of Figure 6 shows, there is very little systematic crosstalk bias between the wind speed error and rain rate below 10 mm/h for either C-, X-, or K-band algorithm.

Figure 7 shows scatterplots of wind speeds from HRD and the three WindSat H-wind algorithms as well as NCEP GDAS, respectively. The plots also list bias and standard deviation of the difference between WindSat/NCEP and HRD wind speed as well as the Pearson correlation coefficient and shows the best linear fits. The value of the standard deviation has been corrected for the sampling mismatch error (section II.E). The figure shows that the all three H-wind algorithms produce much better wind speeds than the NCEP GDAS field. As it is obvious from Figure 4 (d), the NCEP GDAS analysis places the hurricane approximately at the right location but it tends to strongly underestimates the wind speed in the eye of the storm.

VII. GLOBAL WIND SPEED ALGORITHM

The next step is the development of a the global wind speed algorithm, which can retrieve wind speeds in rain under all conditions and at all locations and times. This is a much more challenging task than the development of the H-wind algorithm, which is only designed to be applied in tropical cyclones. The high variability of rain can effect the various channels differently in the tropics than it does at mid or high latitudes. Therefore we cannot expect the same accuracy for the global wind speed algorithm as for the H-wind algorithm.

The regression of the global wind speed algorithm has the form:

$$W = a(\tau_{10.7\text{GHz}}, T_S) + b(\tau_{10.7\text{GHz}}, T_S) \cdot T_S + \sum_j c_j(\tau_{10.7\text{GHz}}, T_S) \cdot (T_{B,j} - 150\text{K}) + \sum_j d_j(\tau_{10.7\text{GHz}}, T_S) \cdot (T_{B,j} - 150\text{K})^2 \quad (16)$$

The sum \sum_j runs over all channels in the frequency bands that are to be utilized by the algorithm including the polarimetric channels. The regression coefficients a , b , c_j , d_j depend on the 10.7 GHz transmittance $\tau_{10.7\text{GHz}}$ and the sea surface temperature T_S . Separate algorithms are

trained in each 2-dimensional $[\tau_{10.7\text{GHz}}, T_s]$ interval. When running the algorithm, the value for $\tau_{10.7\text{GHz}}$ is calculated from (8), while T_s is obtained from the Reynolds OI product [25].

The simplest way to train (16) is to use the WindSat TB – NCEP GDAS wind speed matchups from section II.B, which amounts to a statistical algorithm. This works very well at low wind speeds $W \leq 15\text{m/s}$. However, it fails at higher wind speeds for two reasons: First of all, the NCEP wind speed distribution is getting sparse at higher wind speeds causing the algorithm to be undertrained in these cases. Second, as we have seen in Figure 4 (d) and Figure 7, that NCEP GDAS significantly underestimates the wind speed in tropical cyclones and is therefore is not suited for training a statistical regression algorithm at high wind speeds. For this reason we use a semi-statistical algorithm, which is trained from the synthetic global atmospheric data set of section III.A. This set combines the atmospheric parameters that were derived from actual WindSat measurements with uniform randomly distributed wind speeds and wind directions and the surface emissivity is computed from our RTM. When retrieving wind speeds we compute a first-guess wind speed W' from the semi-statistical algorithm and a wind speed W'' from the statistical algorithm. Both wind speed are blended to obtain the final wind speed W :

$$W = [1 - \Lambda(W')] \cdot W'' + \Lambda(W') \cdot W' \quad (17)$$

The value of the interpolation function $\Lambda(W')$, which depends on the wind speed from the semi statistical algorithm, is 1 at high winds and 0 at low winds and $\Lambda(W')$ is chosen to ensure a seamless transition from low and high wind speeds.

Like we had done for the H-wind algorithm, we train global C-band, X-band and K-band algorithms.

The algorithms are tested with the global WindSat TB – NCEP GDAS wind speed matchups from section II.B. We have again set half of the data set aside for the test runs and have not used it for the training. Table 5 and Table 6 show the biases and standard deviations of the difference between the wind speeds from the retrievals and the NCEP GDAS wind speeds as function of WindSat rain rate and GDAS wind speed, respectively. In Table 5 we have also included the results for the no-rain algorithm. No corrections for sampling mismatch errors were performed, as it is difficult to estimate these error on a global scale. However, one should keep in mind, that part of the errors in Table 5 and Table 6 are due to time or location mismatch between the NCEP

GDAS and the WindSat winds and also that the NCEP GDAS winds themselves are not perfect ground truth data. Like it was the case with the H-wind algorithms, there is no significant degradation of the global X-band algorithm compared with the C-band algorithm if the rain rate is below 5 mm/h and only a moderate degradation in stronger rain. The global K-band algorithm performs much worse than the C-band and X-band algorithms already in light rain.

We have also run the global C-band algorithm on the WindSat brightness temperatures – HRD wind matchup set of section II.C and included the results for in the WindSat pass over hurricane FABIAN in Figure 4 (f) and the results for the whole data set have been included in Figure 6 and Figure 7. As expected, the performance of the global C-band algorithm in tropical cyclones is not as good as the performance for the C-band H-wind algorithm, which has been specifically trained in those conditions. The cases where the global algorithm either over or undercorrects are more noticeable compared with the H-wind algorithm. However, the global C-band algorithm clearly outperforms the no-rain algorithm and its wind speeds are also much better than the ones from NCEP GDAS.

Finally we should note that we have not used any HRD wind speeds in the training of the global wind speed algorithm, but we have relied on simulated brightness temperatures that used the physical emissivity model of section IV. In this model the wind induced emissivity [2] has been linearly extrapolated from 18 m/s to higher wind speeds. Any bias in this emissivity model would show up as bias in the retrieved wind speed when we compare them to the HRD wind speeds. The absence of such biases in the scatterplot for the global algorithm in Figure 7 (d) for wind speeds below 35 m/s indicates that this linear extrapolation is indeed justified.

VIII. WIND DIRECTION RETRIEVALS

Our study of wind direction retrievals focuses on hurricanes and wind speeds above 8 m/s. Even in rain free atmospheres accurate radiometer wind direction measurements at low wind speeds are difficult because of the small wind direction signal in the surface emissivity. In rainy atmospheres we expect the signal at low wind speeds to be even weaker due to the increased atmospheric attenuation.

The wind direction retrieval algorithm in rain follows the same procedure than for rain free atmospheres [2]. The first step is to retrieve wind speed W using the H-wind algorithm (section VI)

and the atmospheric transmittance τ using the auxiliary atmospheric algorithm (section III.B). The results that we will present in this section have been obtained with X-band algorithms. The values for W and τ are inputs to a maximum likelihood estimate (MLE), which minimizes the weighted sum of squares between measured and RTM brightness temperatures as function of wind direction φ . Whereas the rain free wind direction retrieval [2] utilized appropriate combinations between V-pol and H-pol channels as well as the 3rd (S3) and 4th (S4) Stokes parameters, our wind direction retrieval algorithm in rain will utilize only S3 and S4. The reason for this change from the rain free wind direction retrieval is that using V-pol or H-pol observations would require an accurate knowledge of the atmospheric parameters τ , T_{BU} and T_{BD} in order to compute the large isotropic part of the brightness temperature (2). In rainy atmospheres it is difficult to retrieve those parameters to the necessary level of accuracy.

The MLE results in a set of 1 – 4 solutions (ambiguities). For selecting an ambiguity we pass the ambiguity array for each orbit through a circular vector median filter (MF) as it has been described in [2].

Figure 8 displays the RMS between the wind direction from our retrieval and the HRD wind direction for the storms in set in section II.C as function of rain rate. The estimated sampling mismatch error has been removed as explained in section II.E. The statistics for the ambiguity from the MLE, which is closest to the HRD wind vector is shown as dashed line and the ambiguity that is selected by the MF is shown as full line. As expected, the performance of the algorithm degrades with increasing rain rate, because the signal strength (9) decreases with increasing atmospheric attenuation. The degradation is very gradual until the rain rate exceeds 7 mm/h. In heavy rain the signal to noise ratio is getting so small that accurate wind direction retrievals become difficult or impossible.

IX. COMPARISON OF RADIOMETER AND SCATTEROMETER WIND VECTOR RETRIEVALS IN RAIN

Our comparison of hurricane wind speed and direction measurements by radiometers and scatterometers in rainy atmospheres is based on the set of triple matchups between WindSat, QuikSCAT and HRD wind vectors from section II.D. This way we perform a one by one comparison of the two satellite wind vectors. Rather than calculating separate statistics from different Wind-

sat – HRD and QuikSCAT – HRD matchup sets we use only data where there exists a WindSat and QuikSCAT observation at the same location within a small time window. The WindSat H-wind retrievals are done with the X-band algorithm. Its resolution (LR) matches approximately the resolution of the QuikSCAT swath data.

The main goal of our study is to assess how the performance of both instruments degrades with increasing rain rate. Figure 9 displays wind vector fields of the HRD analysis, the QuikSCAT JPL algorithm, our WindSat X-band H-wind algorithm together with the WindSat rain rate for hurricane FABIAN (04 September 2003).

Figure 10 shows scatterplots of wind speeds from HRD, from the WindSat H-wind X-band algorithm and from JPL QuikSCAT for three different rain rate intervals. The figure also lists bias and standard deviation of the difference between satellite (WindSat or QuikSCAT) and HRD wind speed as well as the Pearson correlation coefficient and shows the best linear fits. The value of the standard deviation has been corrected for the sampling mismatch error (section II.E). Both instruments perform equally well without any noticeable biases if there is no rain present. If there is rain in the atmosphere, the wind speeds of the WindSat H-wind X-band algorithm are higher than the HRD wind speeds at low wind speed (< 12 m/s), whereas at high wind speeds (> 30 m/s) the WindSat wind speeds are slightly lower than the HRD winds. This is consistent with the observation of section VI about the H-wind algorithm over or under correcting for the rain effect in certain cases depending on wind speed and rain rate. For wind speeds between 12 m/s and 30 m/s there is no noticeable bias between WindSat and HRD wind speeds. Even in light rain, the JPL QuikSCAT wind speeds are biased high compared with both the HRD and the WindSat H-winds by about 2 – 3 m/s over the whole wind speed range below 30 m/s. At high winds the JPL QuikSCAT wind speeds are lower than the HRD analysis winds. In rain, the standard deviation of the QuikSCAT wind speeds is slightly larger than the one of the WindSat H-winds. It might be possible to improve the performance of the scatterometer wind speeds by training the scatterometer retrieval algorithm for hurricane conditions, which has not been done yet. Of course, any rain correction to the scatterometer wind speeds would require a space-time collocated radiometer measurement of the rain rate. We also want to note that part of the scatter in Figure 10 is due to the sampling mismatch error that is present when comparing radiometer and scatterometer winds with the HRD wind speed analysis, as we have discussed in section II.E.

The RMS for the wind direction differences between satellite and HRD winds as function of

rain rate for wind speed above 8 m/s are shown in Figure 11. Note that the data sets of section II.D is a subset of the data set of section II.C. Therefore we do expect small differences in the WindSat – HRD statistics when comparing Figure 8 with Figure 11. The RMS accuracy of the selected WindSat wind direction ambiguity is comparable to the one from JPL QuikSCAT if the rain rate is below 7 mm/h. The scatterometer shows a degradation already at light rain but the RMS accuracy stays almost constant with increasing rain rate and does not significantly decrease even in heavy rain. The degradation of the radiometer wind direction accuracy with increasing rain rate is more gradually. As we have already seen in section VIII, the radiometer wind direction accuracy decreases strongly in heavy rain because of the strong attenuation of the signal. This is also clearly visible in Figure 9 from the noisy WindSat wind vectors in areas with heavy rain. Finally we want to note that at low wind speeds the wind direction retrieval performance of the scatterometer is significantly better than the one of the radiometer, because at low wind speeds the radiometer surface wind direction signal fades out whereas the scatterometer signal does not.

X. SUMMARY AND CONCLUSIONS

The algorithms for retrieving wind speeds in rain are based on the spectral differences of the wind and rain signals, which makes it possible to find combinations between channels of different frequency bands that can reduce the impact of rain on the brightness temperatures but still keep sufficient sensitivity to wind speed. We have found no indication for a decrease or saturation of the wind speed signal in the brightness temperatures at wind speeds up to 35 m/s. This allows retrievals of wind speeds in hurricanes even under heavy rain. Because of the difficulty to accurately model brightness temperatures in rainy atmospheres, it is necessary to use a statistical algorithm, which has to be trained post-launch from actual observations instead of a physical algorithm that can be trained pre-launch from simulated brightness temperatures.

We have trained H-wind speed retrieval algorithms that work specifically conditions present in tropical cyclones. If C-band channels and higher frequencies are available the estimated RMS accuracy of the retrieved H-wind speeds ranges from about 2.0 m/s in light rain to about 4.0 m/s in heavy rain. If only X-band and higher frequencies are available, the estimated RMS accuracy ranges from about 2.0 m/s in light rain to about 5.0 m/s in heavy rain. If neither C-band nor X-band frequencies are available, the estimated RMS accuracy ranges from about 3.0 m/s in light

rain to about 6.0 m/s in heavy rain.

We have also trained a global wind speed retrieval algorithm, which can be applied in all rainy atmospheres over the whole Earth. It is a semi-statistical algorithm, which combines atmospheric properties that are obtained from actual measurements with simulated surface emission. The estimated RMS accuracy of the global algorithm ranges from about 2.0 m/s in light rain to about 5.0 m/s in heavy rain, if C-band channels and higher frequencies are available. If only X-band channels and higher frequencies are available, the estimated RMS accuracy ranges from about 2.0 m/s in light rain to about 6.0 m/s in heavy rain. It seems that accurate global wind speed retrievals in rain are not possible if the radiometer has neither C-band nor X-band channels.

Though our study was based on WindSat measurements, similar H-wind and global wind speed retrieval algorithms in rain with similar expected performances can be developed for other microwave radiometers, which measure at the same frequency bands as WindSat, such as for example the Advanced Microwave Scanning Radiometer (AMSR) or TMI. An H-wind algorithm but not a global wind speed algorithm could be developed for SSM/I or SSMIS. Because all these instruments measure brightness temperatures at different frequencies, incidence angles and resolutions, it will be necessary to retrain each algorithm specifically for each sensor.

Finally, we have demonstrated that the wind direction signal in the surface emissivity for the 3rd and 4th Stokes parameter is strong enough to measure wind directions in hurricanes with a polarimetric radiometer like WindSat to a similar accuracy than the scatterometer does, provided that the wind speed is larger than 8 m/s and the rain rate does not exceed 7 mm/h. The dominant signal is in the 3rd Stokes parameter.

TABLES

	Storm Name	Storm ID	Year	HRD Time	Approximate WindSat Time	Approximate QuikSCAT Time	Longitude Shift [°]	Latitude Shift [°]
1	ERIKA	al08	2003	08/15 13:30	08/15 12:30		0	0
2	ERIKA	al08	2003	08/16 01:30	08/16 00:00	08/16 00:30	- 0.875	+ 0.375
3	ERIKA	al08	2003	08/16 10:30	08/16 12:30	08/16 11:00	0	0
4	FABIAN	al10	2003	09/03 07:30	09/03 10:30		+ 0.375	0.75
5	FABIAN	al10	2003	09/03 19:30	09/03 21:45		0	- 0.5
6	FABIAN	al10	2003	09/04 07:30	09/04 10:15	09/04 10:00	0	- 0.375
7	ISABEL	al13	2003	09/14 07:30	09/14 10:45		0.5	- 0.25
8	ISABEL	al13	2003	09/14 19:30	09/14 22:00		0	0
9	ISABEL	al13	2003	09/17 13:30	09/17 11:20		- 0.25	0
10	ISABEL	al13	2003	09/17 22:30	09/17 22:45	09/17 23:00	0	0
11	ISABEL	al13	2003	09/18 10:30	09/18 11:10	09/18 11:00	0	- 0.5
12	BONNIE	al02	2004	08/10 13:30	08/10 11:30	08/10 12:00	0	0
13	FRANCES	al06	2004	09/04 09:00	09/04 11:15		0	0
14	FRANCES	al06	2004	09/04 21:00	09/04 22:30		0	0
15	IVAN	al09	2004	09/14 21:00	09/14 22:50		0	- 0.5
16	JEANNE	al11	2004	09/25 21:00	09/25 23:00		+ 0.5	0
17	JEANNE	al11	2004	09/26 09:00	09/26 11:30		0	0

Table 1: HRD – WindSat (section II.C) and HRD – WindSat – QuikSCAT (section II.D) matchups. The table lists the storm name, the storm ID of the National Hurricane Center, year, date (month/day) and UTC time (hour:minute) of the HRD analysis as well as date and approximate time of the WindSat and QuikSCAT overpasses. The last two columns contain the shift in longitude and latitude (in °) of the resampled HRD which makes the storm eyes of the HRD analysis and the two satellite measurement coincide.

HRD wind speed bin m/s	Population	Average WindSat rain rate mm/h	Average atmospheric transmittance τ				
			6.8 GHz	10.7 GHz	18.7 GHz	23.8 GHz	37.0 GHz
[0, 5[4701	0.1	0.980	0.975	0.845	0.642	0.773
[5, 10[14759	0.3	0.979	0.969	0.831	0.627	0.757
[10, 15[13371	0.4	0.975	0.963	0.815	0.605	0.737
[15, 20[7237	1.7	0.960	0.927	0.730	0.517	0.617
[20, 25[4393	3.0	0.942	0.883	0.635	0.430	0.493
[25, 30[2338	4.9	0.922	0.826	0.530	0.347	0.378
[30, 35[1118	6.7	0.906	0.777	0.441	0.280	0.284
[35, 40[607	7.8	0.894	0.747	0.388	0.243	0.240
> 40	166	11.0	0.859	0.646	0.286	0.190	0.193

Table 2: Population, average rain rate and average values of τ as function of wind speed for the WindSat TB – HRD wind vector collocations of section II.C.

Data Set	Average	Estimated Wind Speed	Estimated Wind Speed
----------	---------	----------------------	----------------------

	Time Difference [sec]	Sampling Mismatch RMS Error [m/s]	Sampling Mismatch RMS Error [deg]
WindSat – HRD (section II.C)	8100	1.7	17
WindSat – HRD (section II.D)	7000	1.6	16
QuikSCAT – HRD (section II.D)	6300	1.5	15

Table 3: Average time differences and estimated RMS sampling mismatch errors in wind speed and wind direction for the study data sets of section II.

Number of events	no rain algorithm		6 H – 0.3 * 10 H algorithm		H wind algorithm C-band	
	Bias	Standard Deviation	Bias	Standard Deviation	Bias	Standard Deviation
	m/s	m/s	m/s	m/s	m/s	m/s
48690	9.4	15.1	0.9	3.7	-0.3	2.5

Table 4: Bias and standard deviation of the differences between the wind speeds from the WindSat algorithm that is trained without rain, a simple regression using the channel combination 6H – 0.3*10H, the WindSat H-wind algorithm utilizing C-band and higher frequencies and the scaled and resampled HRD wind speed from the data set of section II.C. The sampling mismatch error (section II.E) has been removed in the standard deviation error.

SSM/I rain interval	average SSM/I rain rate	Population	global algorithm C-band		global algorithm X-band		global algorithm K-band		no rain algorithm	
			Bias	SDEV	Bias	SDEV	Bias	SDEV	Bias	SDEV
mm/h	mm/h		m/s	m/s	m/s	m/s	m/s	m/s	m/s	m/s
]0, 2]	0.7	887091	0.2	2.0	0.2	2.0	2.4	4.8	5.9	5.5
]2, 4]	2.8	254702	0.5	2.5	0.6	2.6	6.1	6.7	12.8	9.7
]4, 6]	4.8	99053	0.9	2.9	1.1	3.3	9.0	7.3	19.8	12.9
]6, 8]	6.8	47020	1.3	3.4	1.8	4.0	10.7	7.2	27.8	15.9
above 8	10.6	55161	2.4	4.6	3.3	5.7	12.4	7.0	41.6	21.3

Table 5: Bias and standard deviation (SDEV) of the differences between the WindSat wind speed that is retrieved from the global algorithms utilizing C-band and higher frequencies, X-band and higher frequencies, K-band and higher frequencies, the WindSat algorithm that is trained without rain and the NCEP GDAS wind speed for the data set of section II.B. The results are stratified as function of the SSM/I rain rate.

			global	global	global
--	--	--	--------	--------	--------

NCEP wind speed interval	average NCEP wind speed	Population	algorithm C-band		algorithm X-band		algorithm K-band	
			Bias	SDEV	Bias	SDEV	Bias	SDEV
m/s	m/s		m/s	m/s	m/s	m/s	m/s	m/s
[0, 5[3.8	260066	1.9	2.5	2.0	2.7	4.3	5.9
[5, 10[7.5	1123821	0.3	1.9	0.4	2.2	3.9	6.0
[10, 15[12.0	485835	-0.3	2.2	-0.2	2.3	2.6	5.6
[15, 20[16.5	87907	-0.1	2.6	-0.2	2.7	2.3	5.9
[20, 25[21.4	3577	0.4	4.0	0.3	3.9	3.2	6.6
[25, 30[27.0	254	-2.3	6.4	-3.3	6.9	5.8	6.7

Table 6: Bias and standard deviation (SDEV) of the differences between the WindSat wind speed that is retrieved from the global algorithms utilizing C-band and higher frequencies, X-band and higher frequencies, K-band and higher frequencies and the NCEP GDAS wind speed for the data set of section II.B. The results are stratified as function of the NCEP GDAS wind speed.

FIGURES

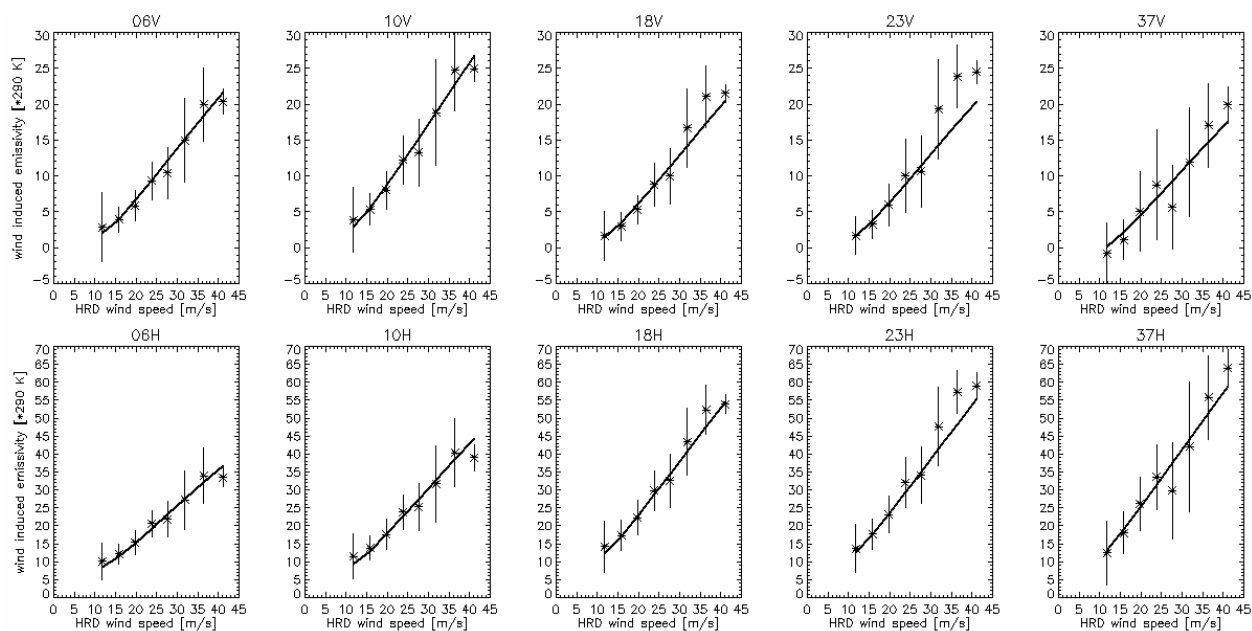


Figure 1: Wind induced sea surface emissivities of all ten WindSat V-pol and H-pol channels as function of surface wind speed. The wind speeds are the scaled and resampled HRD wind speeds from the data set of section II.C. The stars are emissivity values from section IV.B. The solid lines are the emissivity values from [2] that were linearly extrapolated from 18 m/s to higher wind speeds. The emissivities were multiplied with a typical surface temperature of 290 Kelvin.

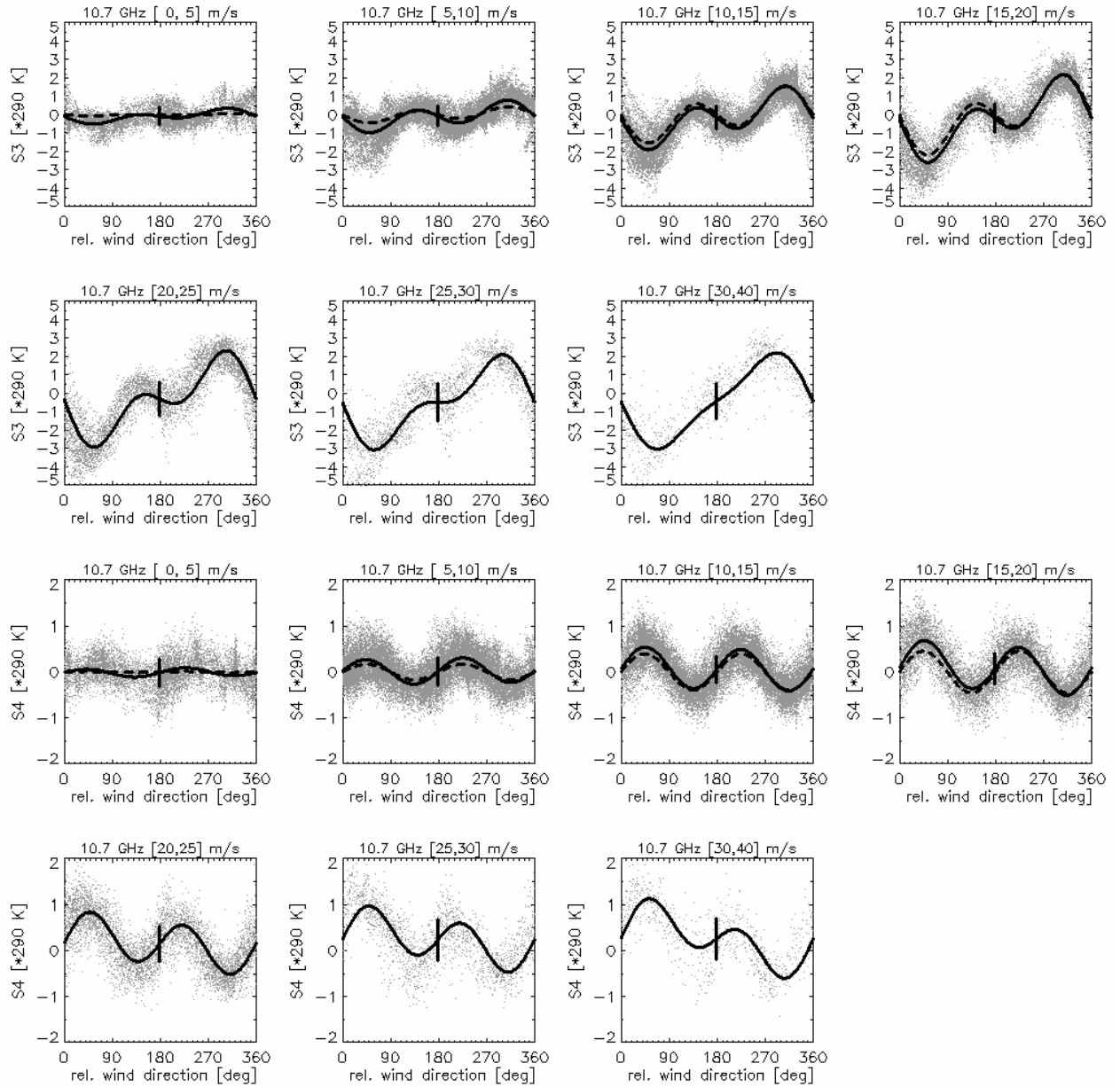


Figure 2: Wind direction signal of the 3rd (S3) and 4th (S4) Stokes parameter at 10.7 GHz as function of wind direction relative to the azimuthal look for seven wind speed bins. The wind speeds and wind directions are the scaled and resampled HRD wind vectors from the data set of section II.C. The emissivities were multiplied with a typical surface temperature of 290 Kelvin. The solid lines are the harmonic fits to the data in each bin. The vertical bars indicate the standard deviation between the data points and the harmonic fit. The dashed lines are the harmonic fits from [2].

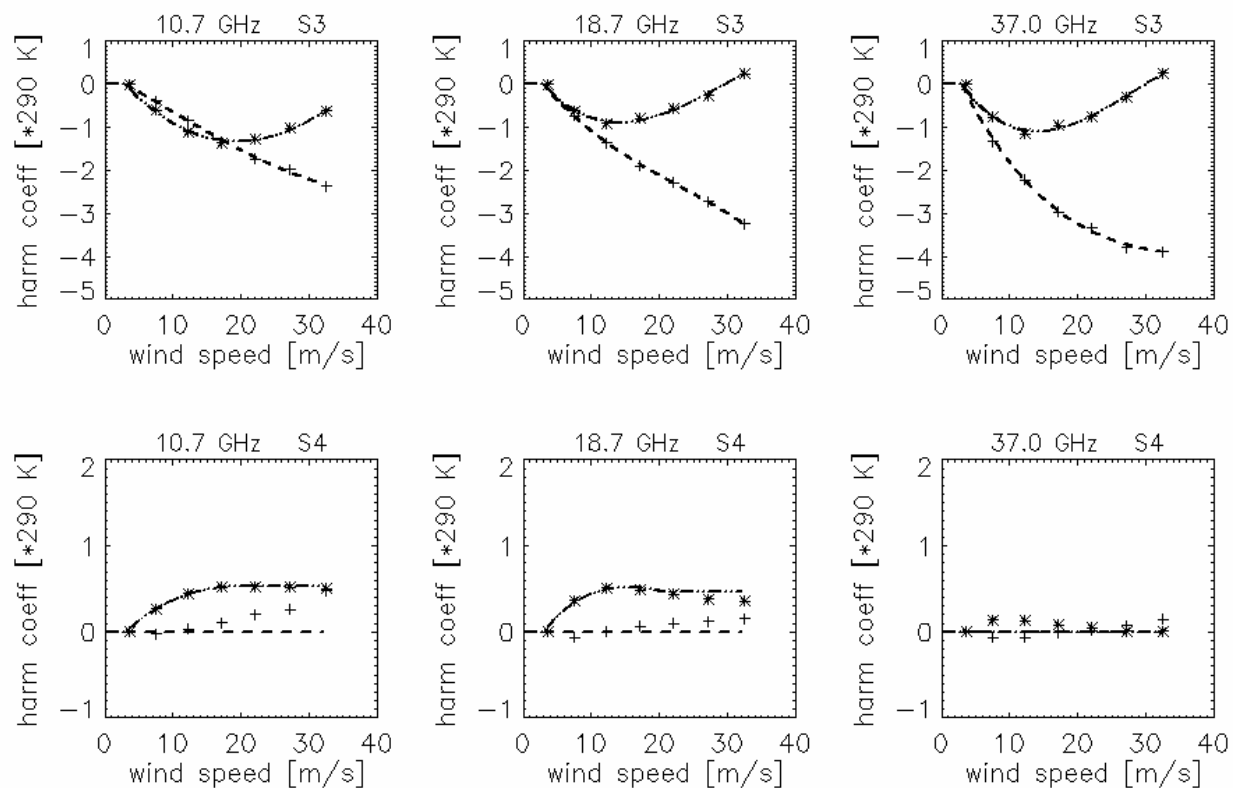


Figure 3: 1st (asterisks) and 2nd (crosses) harmonic coefficients for the 3rd (S3) and 4th (S4) Stokes parameters of the wind direction signal as function of surface wind speed at 10.7, 18.7 and 37.0 GHz. The emissivities were multiplied with a typical surface temperature of 290 Kelvin. The crosses are the measurements that were obtained in this study (section IV.C). The dashed-dot-dot and dashed lines are polynomial fits to these data setting the 1st harmonic of S4 to 0.

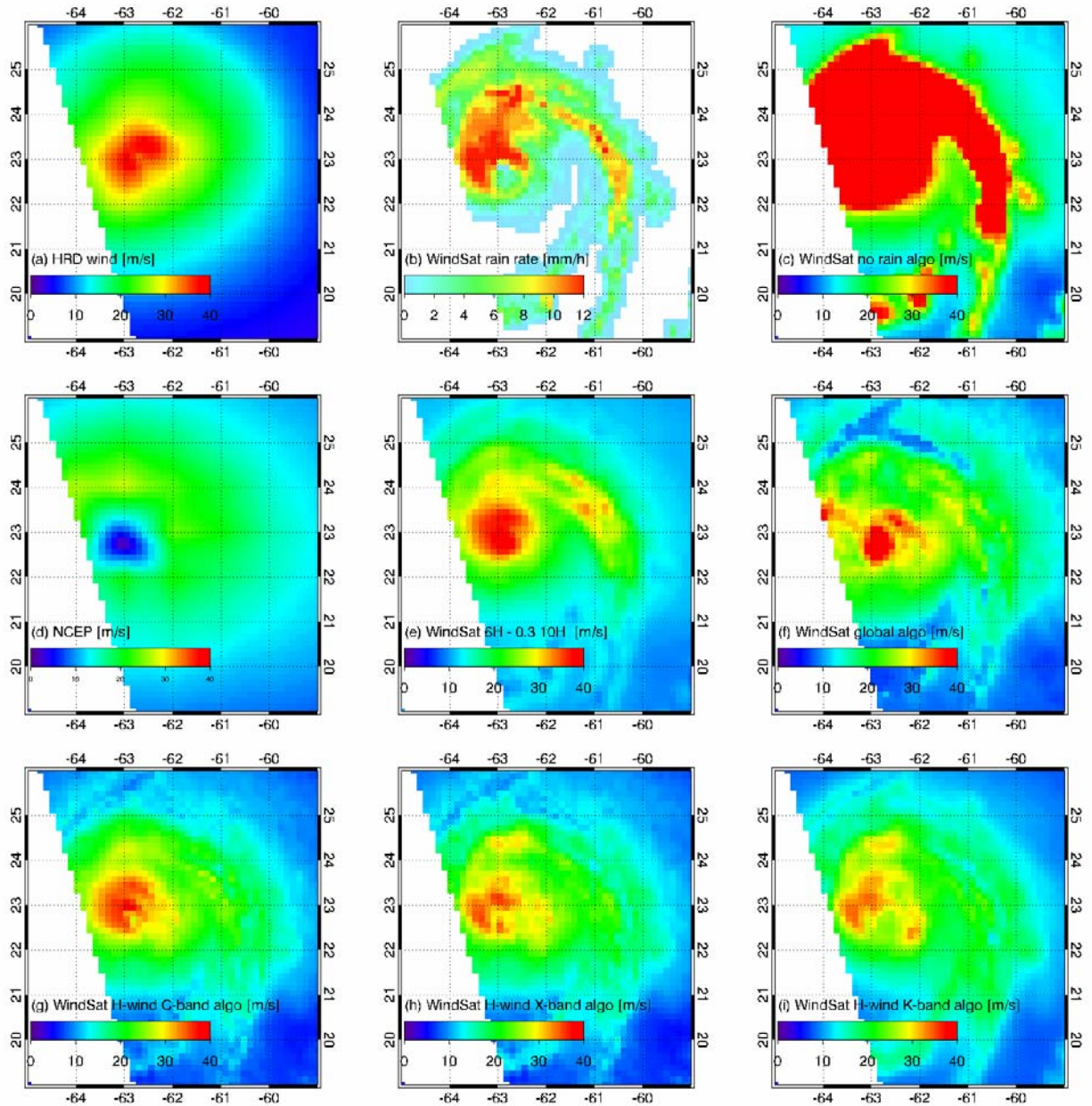


Figure 4: WindSat pass over hurricane FABIAN. The HRD analysis is from 03 September 2003 19:30Z. The time of the WindSat measurement was approximately 21:45Z. The figure shows from top left to bottom right: (a) HRD wind speed after scaling and resampling (c.f. section II.C), (b) WindSat rain rate [mm/h], (c) WindSat wind speed using the standard algorithm that has been trained for rain free atmospheres, (d) NCEP GDAS wind speed (1 deg resolution), (e) WindSat wind speed derived from a simple linear regression using the channel combination $6H - 0.3 * 10H$, (f) WindSat wind speed using the global wind speed algorithm (section VII). The last row shows the WindSat wind speed using the H-wind algorithm: (g) C-band and higher frequencies, (h) X-band and higher frequencies, (i) K-band and higher frequencies.

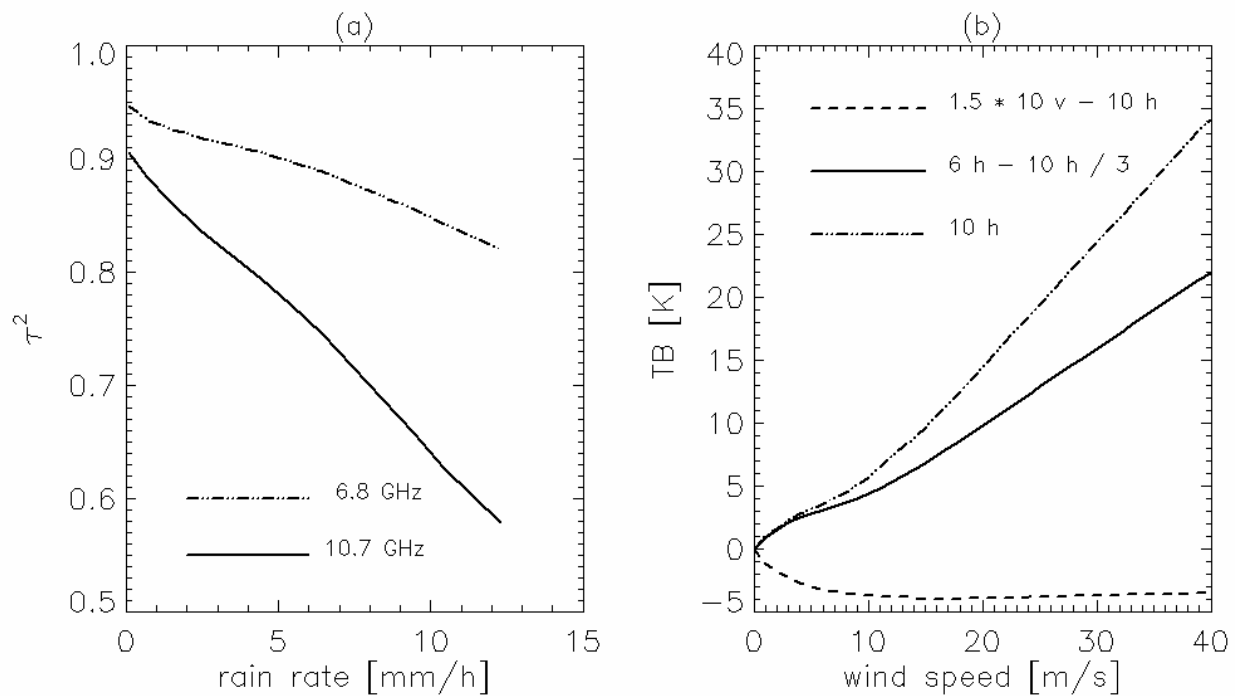


Figure 5: (a) Square of the atmospheric transmittance τ^2 as function of surface rain rate [mm/h] for C-band (dashed-dot-dot) and X-band (solid). The curves have been extracted from the basic ATM set (section III.A). The rain rates were taken from SSM/I F13. (b) Top of the atmosphere brightness temperature [Kelvin] calculated from equation (6) as function of wind speed for various channel combinations: 10 H-pol (dashed-dot-dot), 1.5 * 10 V-pol - 10 H-pol (dashed), 6 H-pol - 1/3 * 10 H-pol (solid). For computing the curves we have used an effective temperature of 283 Kelvin and a surface rain rate of 5 mm/h

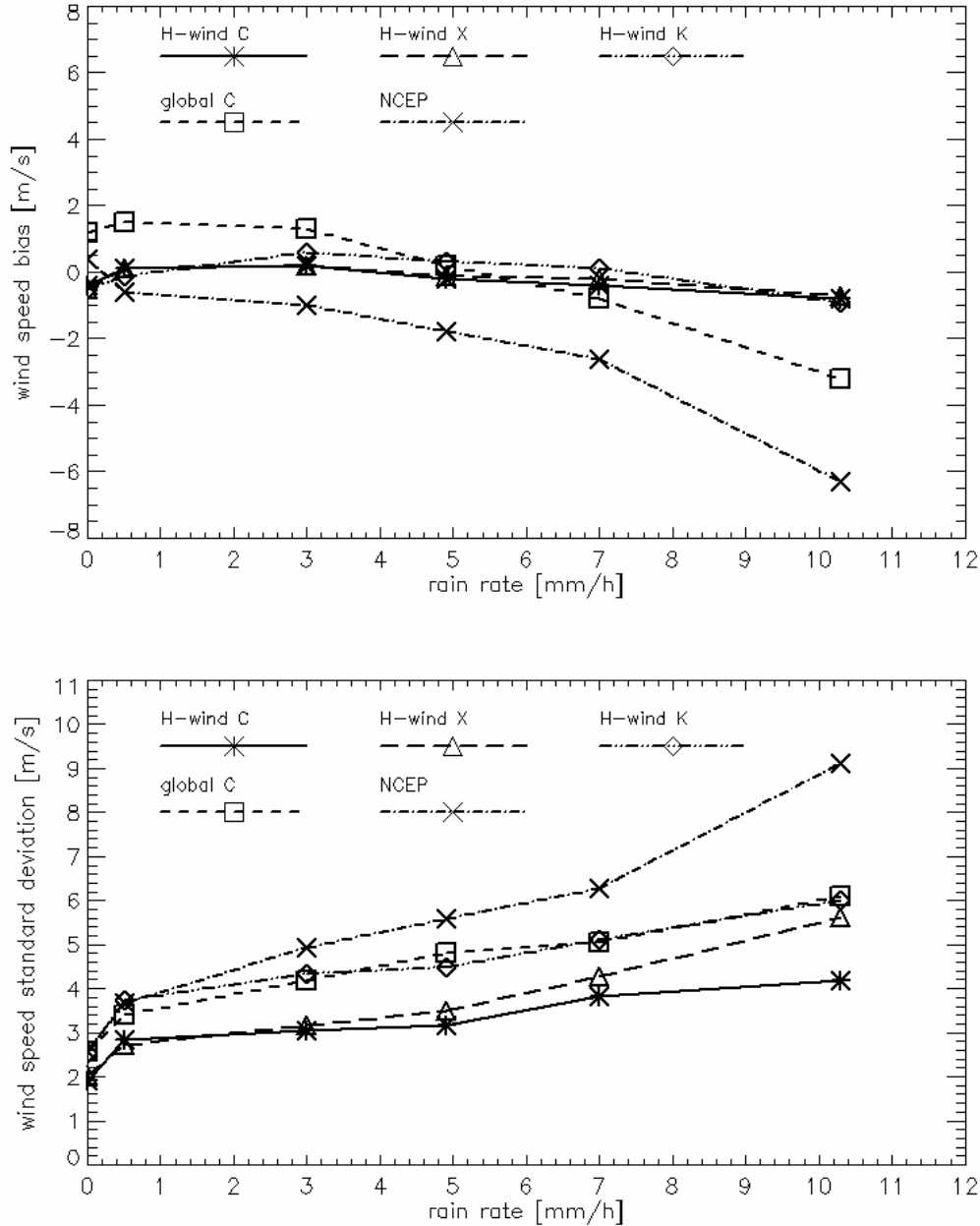


Figure 6: Estimated bias (upper panel) and standard deviation (lower panel) error of the wind speed retrievals in rain as function of surface rain rate: WindSat H-wind algorithm utilizing C-band and higher frequencies (solid line and stars), WindSat H-wind algorithm utilizing X-band and higher frequencies (long dashed line and triangles), WindSat H-wind algorithm utilizing K-band and higher frequencies (dashed-dot-dot lines and diamonds), WindSat global wind speed algorithm utilizing C-band and higher frequencies (short dashed lines and squares), NCEP GDAS (dashed-dot lines and crosses). The figure shows the difference between the various measurements and the scaled and resampled HRD winds [m/s] from data set of section II.C. The estimated sampling mismatch error (section II.E) has been removed. The surface rain rates [mm/h] are WindSat measurements that were retrieved from the UMORA rain retrieval algorithm [3].

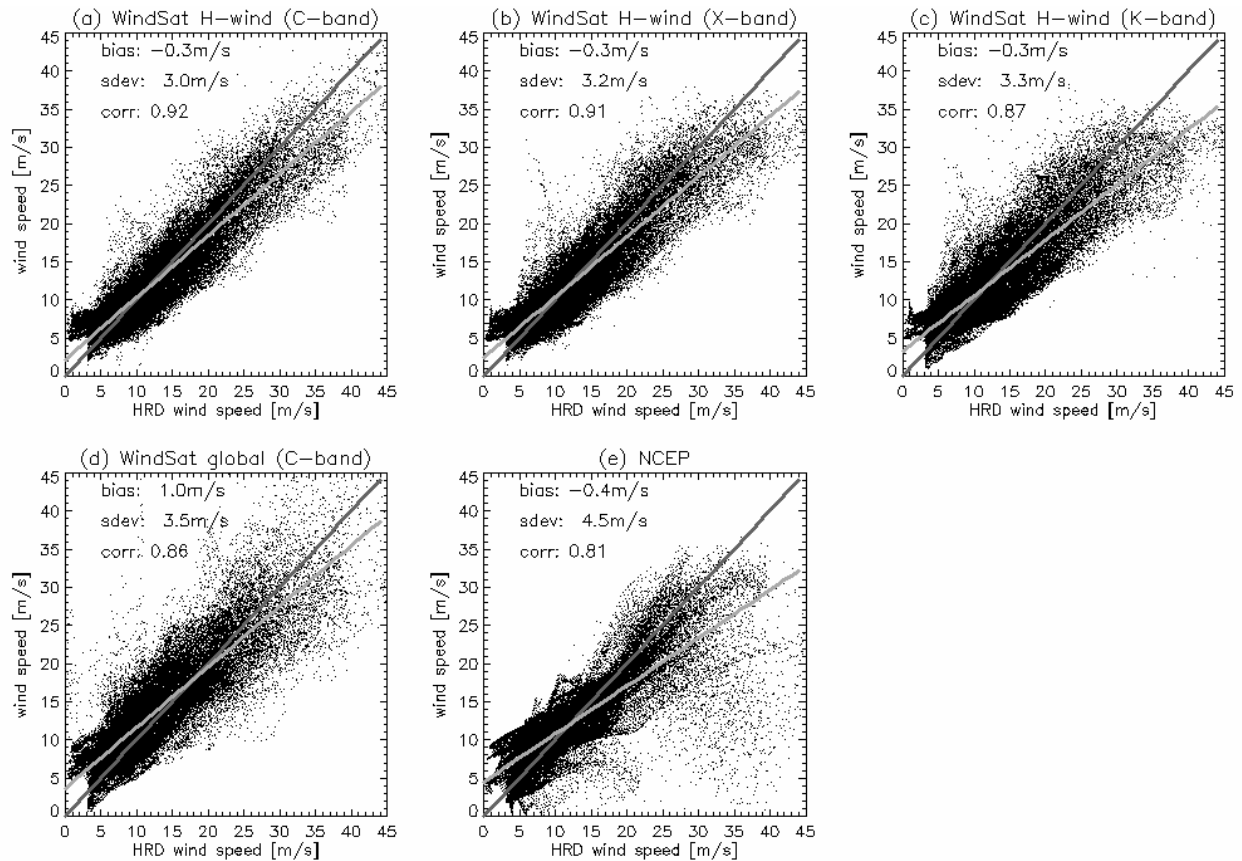


Figure 7: Scatterplots of wind speeds from HRD and the WindSat H-wind algorithm utilizing C-band and higher frequencies (a), X-band and higher frequencies (b), K-band and higher frequencies (c), WindSat global wind speed algorithm utilizing C-band (d) and NCEP GDAS (e), respectively. The data set of section II.C has been used. The plots also list biases and standard deviations (after removing the estimated sampling mismatch error, section II.E) of the differences between WindSat/NCEP and HRD wind speed as well as the Pearson correlation coefficients. The dark grey solid lines indicate the ideal cases. The light grey solid lines indicate the best linear fits.

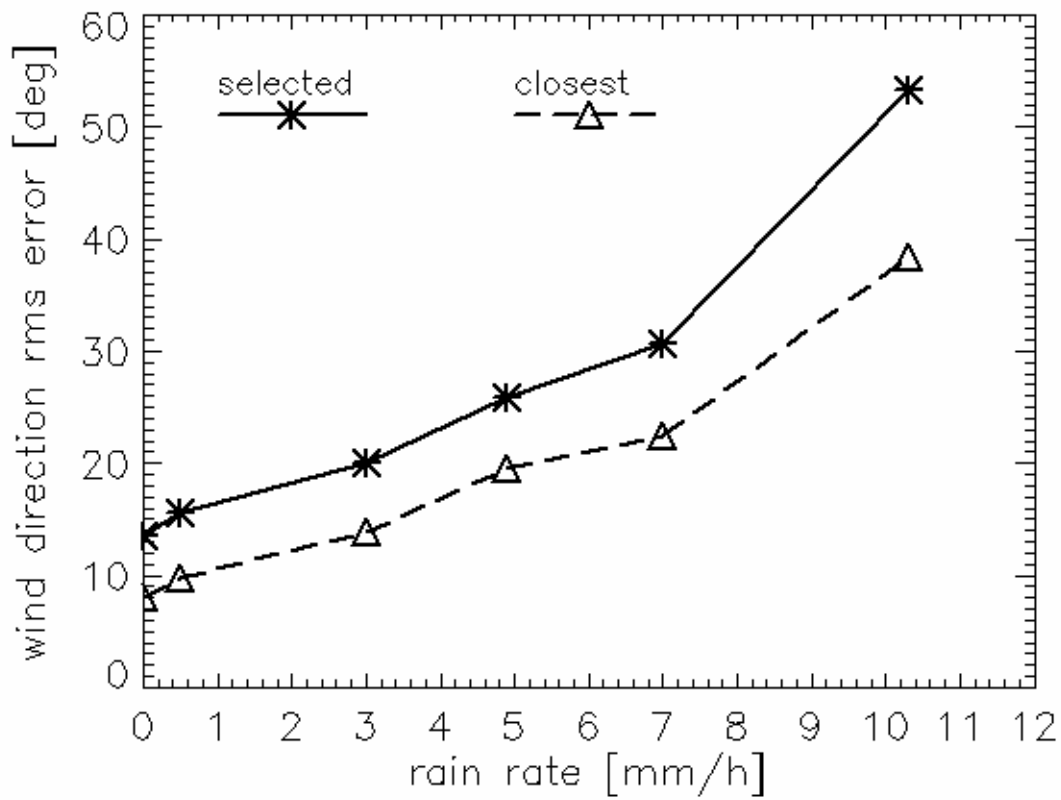


Figure 8: Estimated RMS error of the wind direction retrievals in rain as function of surface rain rate. Only events for which the HRD wind speed exceeds 8 m/s have been included. The errors have been corrected for sampling mismatch errors according to section II.E. The solid line and stars show the error for the WindSat wind vector after the ambiguity selection has been performed. The dashed line and triangles show the error for the WindSat wind vector ambiguity that is closest to the HRD wind vector.

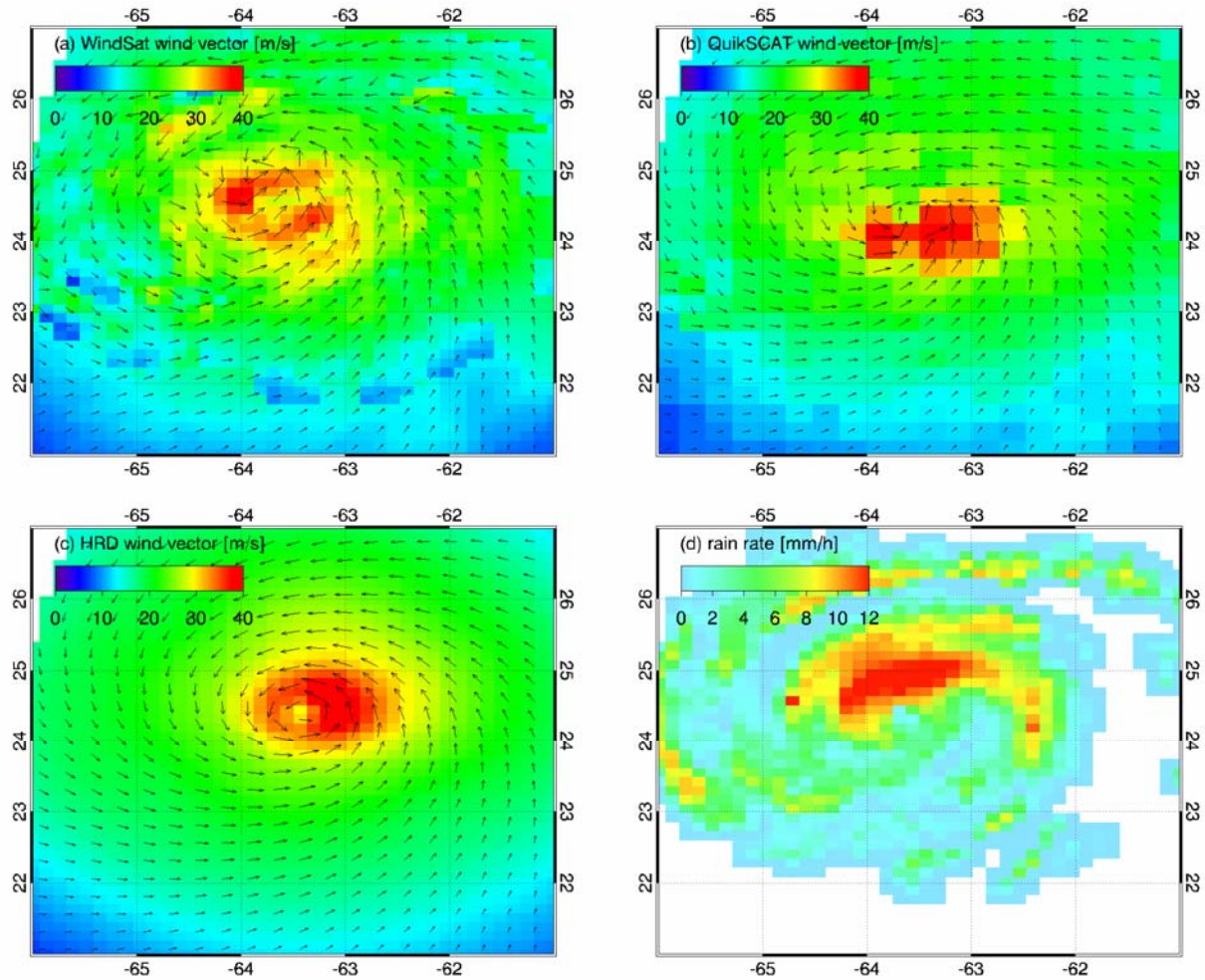


Figure 9: WindSat and QuikSCAT passes over hurricane FABIAN. The HRD analysis is from 04 September 2003 07:30Z. The time of the WindSat measurement was approximately 10:15Z. The time of the QuikSCAT measurement was approximately 10:00Z. The figure shows from top left to bottom right: (a) WindSat H-wind vector utilizing X-band and higher frequencies, (b) JPL QuikSCAT wind vectors, (c) HRD wind speed after scaling and resampling (c.f. section II.C), (d) WindSat rain rate [mm/h]. Only every 2nd wind vector arrow from the data set II.D is plotted.

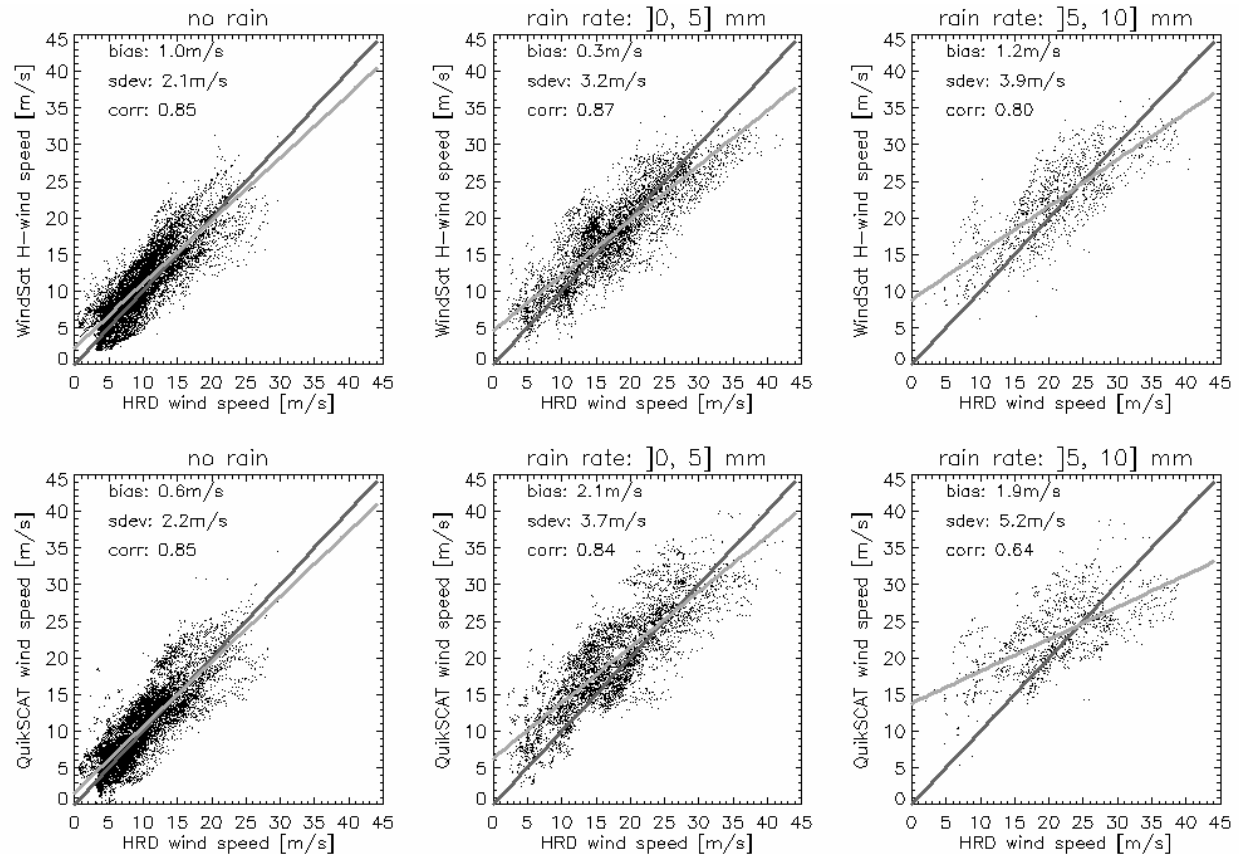


Figure 10: Scatterplots of wind speeds from HRD, the WindSat H-wind utilizing X-band and higher frequencies, and JPL QuikSCAT for 3 different rain rate intervals. The plots also list biases and standard deviations (after removing the estimated sampling mismatch error, section II.E) of the differences between satellite (WindSat or QuikSCAT) and HRD wind speed as well as the Pearson correlation coefficients. The dark grey solid lines indicate the ideal cases. The light grey solid lines indicate the best linear fits.

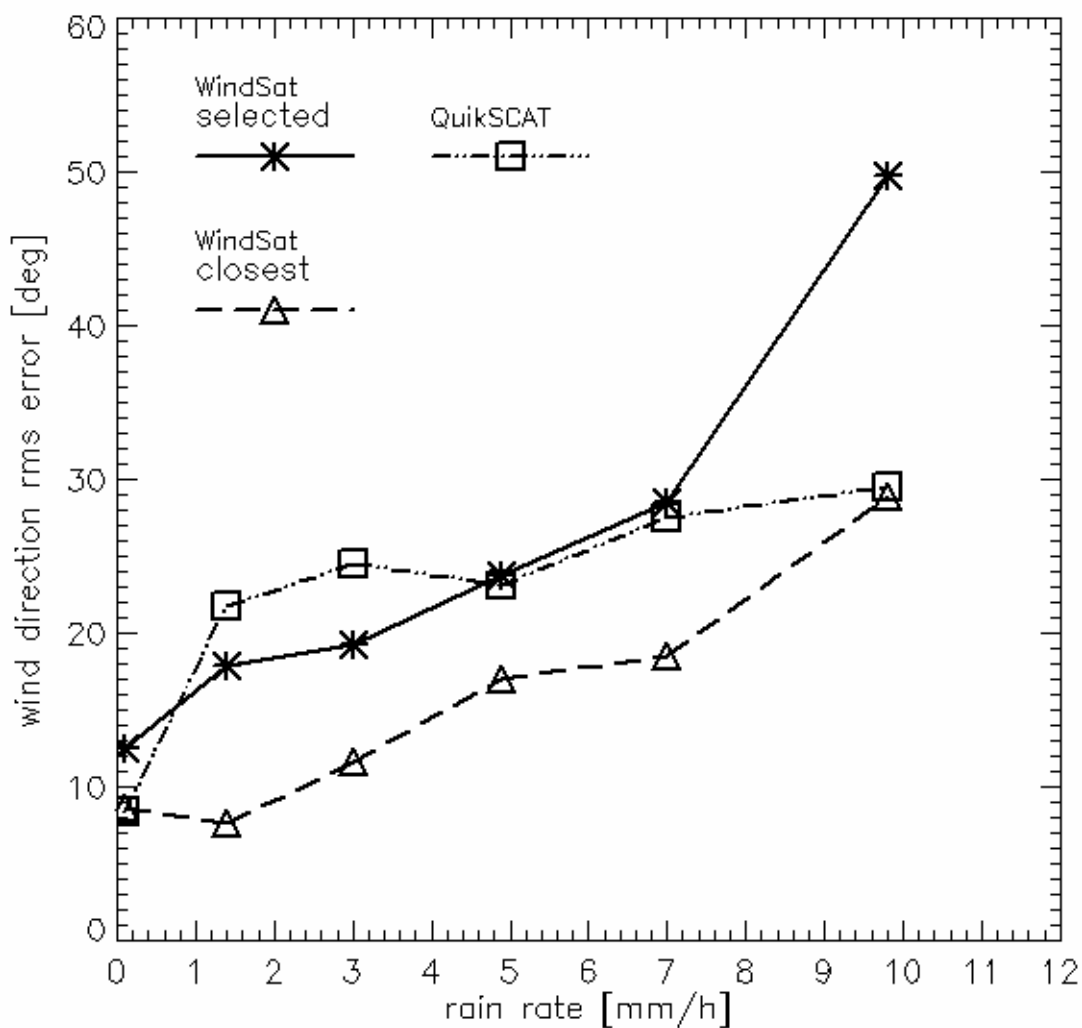


Figure 11: Estimated RMS error of WindSat H-wind directions and JPL QuikSCAT wind direction as function of rain rate: WindSat H-wind vector after ambiguity selection (solid line and stars), WindSat H-wind vector ambiguity that is closest to the scaled and resampled HRD wind vector (dashed line and triangles), QuikSCAT wind vector (dashed-dot-dot line and squares). The figure shows the RMS of the differences between the satellite wind direction measurements and the scaled and resampled HRD wind directions [deg] from the data set of section II.D. Only events for which the HRD wind speed exceeds 8 m/s have been included. The estimated sampling mismatch error (section II.E) has been removed.

Bibliography

- [1] M. H. Bettenhausen, C. K. Smith, R. M. Bevilacqua, N.-Y. Wang, P. W. Gaiser, and S. K. Cox, "A nonlinear optimization algorithm for WindSat wind vector retrievals," *IEEE Transactions on Geoscience and Remote Sensing*, vol. 44, no. 3, pp. 597-608, 2006.
- [2] Meissner, Thomas and Wentz, Frank J., "Ocean retrievals for WindSat: Radiative transfer model, algorithm, validation," presented at the 9th Specialist Meeting on Microwave Radiometry and Remote Sensing Applications, Puerto Rico, USA, 2006, Paper Catalog # 06EX1174C. [Online]. Available: [http://www.remss.com/papers/meissner_and_wentz\(2006\).pdf](http://www.remss.com/papers/meissner_and_wentz(2006).pdf).
- [3] K. A. Hilburn and F. J. Wentz, "Intercalibrated passive microwave rain products from the unified microwave ocean retrieval algorithm (UMORA)," *Journal of Applied Meteorology and Climatology*, vol. 47, pp. 778-794, 2008.
- [4] F. J. Wentz and R. W. Spencer, "SSM/I rain retrievals within a unified all-weather ocean algorithm," *Journal of the Atmospheric Sciences*, vol. 55, no. 9, pp. 1613-1627, 1998.
- [5] K. N. Liou, *An Introduction to Atmospheric Radiation*. New York: Academic Press, 1980.
- [6] W. L. Jones, P. G. Black, V. E. Delnore, and C. T. Swift, "Airborne microwave remote-sensing measurements of hurricane Allen," *Science*, vol. 214, no. 4518, pp. 274-280, 1981.
- [7] E. Knapp, J.R. Carswell, and C. T. Swift, "A dual polarization multi-frequency microwave radiometer," in Proceedings of the 2000 IEEE International Geoscience and Remote Sensing Symposium, Honolulu, HI, USA, 2000, vol. 7, pp. 3160-3162.
- [8] D. W. Draper and D. G. Long, "Evaluating the effect of rain on SeaWinds scatterometer measurements," *Journal of Geophysical Research*, vol. 109, 2004.
- [9] K. A. Hilburn, F. J. Wentz, D. K. Smith, and P. D. Ashcroft, "Correcting active scatterometer data for the effects of rain using passive microwave data," *Journal of Applied Meteorology and Climatology*, vol. 45, pp. 382-398, 2006.
- [10] D. E. Weissman, "Effects of rain rate and wind magnitude on SeaWinds scatterometer wind speed errors," *Journal of Atmospheric and Oceanic Technology*, vol. 19, pp. 738-746, 2002.
- [11] E. Twarog, W. E. Purdy, P. W. Gaiser, K. H. Cheung, and B. E. Kelm, "WindSat on-orbit warm load calibration," *IEEE Transactions on Geoscience and Remote Sensing*, vol. 44, no. 3, pp. 516-529, Mar. 2006.
- [12] G. A. Poe, "Optimum interpolation of imaging microwave radiometer data," *IEEE Transactions on Geoscience and Remote Sensing*, vol. 28, no. 5, pp. 800-810, 1990.

- [13] A. Stogryn, "Estimates of brightness temperatures from scanning radiometer data," *IEEE Transactions on Antennas and Propagation*, vol. AP-26, no. 5, pp. 720-726, 1978.
- [14] T. Meissner and F. J. Wentz, "Polarization rotation and the third stokes parameter: The effects of spacecraft attitude and faraday rotation," *IEEE Transactions on Geoscience and Remote Sensing*, vol. 44, no. 3, pp. 506-515, 2006.
- [15] W. E. Purdy, P. W. Gaiser, G. A. Poe, E. A. Uliana, T. Meissner, and F. J. Wentz, "Geolocation and pointing accuracy analysis for the WindSat sensor," *IEEE Transactions on Geoscience and Remote Sensing*, vol. 44, no. 3, pp. 496-505, 2006.
- [16] J. Hollinger, J. L. Peirce, and G. Poe, "SSM/I instrument description," *IEEE Transactions on Geoscience and Remote Sensing*, vol. 28, no. 5, pp. 781-790, 1990.
- [17] T. Meissner and F. J. Wentz, "A radiative transfer model function for 85.5 GHz Special Sensor Microwave Imager ocean brightness temperatures," *Radio Science*, vol. 38, no. 4, 2003.
- [18] T. Meissner and F. J. Wentz, "The complex dielectric constant of pure and sea water from microwave satellite observations," *IEEE Transactions on Geoscience and Remote Sensing*, vol. 42, no. 9, pp. 1836-1849, 2004.
- [19] M. D. Powell, S. H. Houston, L. R. Amat, and N. Morisseau-Leroy, "The HRD real-time hurricane wind analysis system," *Journal of Wind Engineering and Industrial Aerodynamics*, vol. 77 & 78, pp. 53-64, 1998.
- [20] J.-H. Chu, "Tropical Cyclone Forecasters' Reference Guide," Naval Research Laboratory, Monterey, CA, Reference document initially published as NRL Report NRL/PU/7541--95-0012, October 1995; HTML conversion date: 22 March 1998, 1995. [Online]. Available: <http://www.nrlmry.navy.mil/%7Echu/index.html>.
- [21] M. W. Spencer, C. Wu, and D. G. Long, "Improved resolution backscatter measurements with the SeaWinds pencil-beam scatterometer," *IEEE Transactions on Geoscience and Remote Sensing*, vol. 38, no. 1, pp. 89-104, 2000.
- [22] T. Lungu and P. S. Callahan, "QuikSCAT science data product user's manual: Overview and geophysical data products," Jet Propulsion Laboratory, Pasadena, CA, D-18053-Rev A, Version 3.0, 2006. [Online]. Available: ftp://podaac.jpl.nasa.gov/pub/ocean_wind/quikscat/doc/QSUG_v3.pdf.
- [23] F. J. Wentz and T. Meissner, "AMSR Ocean Algorithm, Version 2," Remote Sensing Systems, Santa Rosa, CA, 121599A-1, 2000. [Online]. Available: http://www.remss.com/papers/amsr/AMSR_Ocean_Algorithm_Version_2.pdf.
- [24] K. N. Liou, "Absorption and Scattering of Solar Radiation in the Atmosphere," in *An Introduction to Atmospheric Radiation*, vol. 84, International Geophysics Series, Second Edition ed. New York: Academic Press, 1980, ch. 3, pp. 65-115.
- [25] R. W. Reynolds and T. M. Smith, "Improved global sea surface temperature analyses using optimum interpolation," *Journal of Climate*, vol. 7, pp. 929-948, 1994.

- [26] T. Meissner and F. J. Wentz, "An updated analysis of the ocean surface wind direction signal in passive microwave brightness temperatures," *IEEE Transactions on Geoscience and Remote Sensing*, vol. 40, no. 6, pp. 1230-1240, 2002.
- [27] S. H. Yueh, "Directional signals in Windsat observations of hurricane ocean winds," *IEEE Transactions on Geoscience and Remote Sensing*, vol. 46, no. 1, pp. 130-136, 2008.
- [28] S. H. Yueh, W. Wilson, S. J. Dinardo, and F. K. Li, "Polarimetric microwave brightness signatures of ocean wind directions," *IEEE Transactions on Geoscience and Remote Sensing*, vol. 37, no. 2, pp. 949-959, 1999.